LTP Modeling and Stability Assessment of Multiple Second-Order Generalized Integrator-Based Signal Processing/Synchronization Algorithms and Their Close Variants

Saeed Golestan, *Senior Member, IEEE*, Josep M. Guerrero, *Fellow, IEEE*, Abdullah M. Abusorrah, *Senior Member, IEEE*, Juan C. Vasquez, *Senior Member, IEEE*, and Yusuf Al-Turki, *Senior Member, IEEE*

***Abstract*—A second-order generalized integrator (SOGI) is a resonant regulator with a pair of complex-conjugate poles, and therefore, with infinite magnitude at its center frequency. Thanks to this property, one can put together a set of m SOGIs in an elegant way and decompose a single-phase signal into its constituent frequency components and detect their amplitude and phase angle. Such a configuration, which is often referred to as the multi-SOGI (MSOGI) structure, requires a frequency estimator to adapt the center frequency of SOGIs to frequency changes. This frequency estimation is often provided by interconnecting the MSOGI structure with a basic frequency-locked loop (FLL) or phase-locked loop (PLL). The resulting structures are known as the MSOGI-FLL and MSOGI-PLL. These structures and their close variants are mathematically difficult to analyze probably because of the lack of a linear model for these systems. This article aims to bridge this research gap. First, it is shown how linear time-periodic (LTP) models of the MSOGI-FLL and MSOGI-PLL can be obtained. The model verification, obtaining open-loop harmonic transfer function from the LTP model, and LTP stability assessment of MSOGI-based synchronization systems are the next parts of this article. Finally, some close variants of the MSOGI-FLL/PLL are considered and their modeling and stability assessment are briefly discussed.**

***Index Terms*—Frequency-locked loop (FLL), linear time-periodic (LTP), modeling, phase-locked loop (PLL), single-phase systems, synchronization.**

Manuscript received September 9, 2021; accepted November 1, 2021. Date of publication November 8, 2021; date of current version January 19, 2022. This work was supported in part by the Deanship of Scientific Research (DSR), King Abdulaziz University, Jeddah, under Grant FP-178-43 and in part by VILLUM FONDEN under VILLUM Investigator Grant 25920: Center for Research on Microgrids (CROM). Recommended for publication by Associate Editor T. Suntio. *(Corresponding author: Saeed Golestan.)*

Saeed Golestan, Josep M. Guerrero, and Juan C. Vasquez are with the The Villum Center for Research on Microgrids (CROM), AAU Energy, Aalborg University, 9220 Aalborg, Denmark (e-mail: sgd@energy.aau.dk; joz@energy.aau.dk; juq@energy.aau.dk).

Abdullah M. Abusorrah and Yusuf Al-Turki are with the Department of Electrical and Computer Engineering, Faculty of Engineering, K. A. CARE Energy Research and Innovation Center, King Abdulaziz University, Jeddah 21589, Saudi Arabia, and also with the Center of Research Excellence in Renewable Energy and Power Systems, King Abdulaziz University, Jeddah 21589, Saudi Arabia (e-mail: yaturki@yahoo.com; aabusorrah@kau.edu.sa).

Color versions of one or more figures in this article are available at https://doi.org/10.1109/TPEL.2021.3125743.

Digital Object Identifier 10.1109/TPEL.2021.3125743

I. Introduction

MOTIVATED by both political and environmental concerns and facilitated by recent scientific/engineering advances, the share of renewable energy sources, especially photovoltaic and wind systems, in the generation of electricity is significantly growing [1]. This fast movement toward low-carbon energy generation, however, is not without a problem. The main challenge is probably having a so-called *low-inertia* power system, which is characterized by abrupt frequency changes, increased harmonic distortions, and reduced stability margin in the system [2]. It implies that in addition to upgrading the control/synchronization systems of power converters to deal with these stability/power quality issues, efficient and reliable algorithms to monitor the grid voltage frequency components may also be required.

To contribute toward addressing the above-mentioned needs, designing multipurpose time-domain signal processing algorithms to undertake the grid synchronization, signal decomposition, and monitoring responsibilities at the same time has received much attention. These algorithms, which can detect the fundamental and a selective number of harmonic components of a power signal, and their phase angle, amplitude, and frequency, may be realized in different ways. The focus of this article is on multiple second-order generalized integrators (MSOGI) based algorithms and their close variants. A SOGI is a resonant regulator with a pair of complex-conjugate poles at a frequency called the center frequency. In what follows, the historical development of the MSOGI-based algorithms is presented.

Research groups with different backgrounds have contributed to developing the SOGI-based synchronization and signal processing algorithms. In the power and energy area, [3] and [4] should be credited for their pioneering works in this area. By including a SOGI centered at the fundamental frequency in a unity feedback loop, they proposed a configuration [today known as the SOGI-based orthogonal signal generator (SOGI-OSG)]. The SOGI-OSG extracts the fundamental component of a single-phase input signal and generates a fictitious component orthogonal to the fundamental one, which can be used for determining the fundamental phase angle and amplitude of

the input signal. It, however, has a number of problems, as follows [5].

1) It provides no information about the harmonic content of the input signal.
2) It is nonfrequency adaptive because the SOGI's center frequency is fixed at its nominal value. Therefore, it is only applicable for scenarios where the frequency of the single-phase input signal is fixed at (or very close to) its nominal value.
3) Improving its accuracy is only possible by significantly slowing down the dynamic response.

To provide an estimation of the amplitude and phase angle of fundamental and harmonic components of a single-phase signal at the same time, an MSOGI configuration as shown in Fig. 1(a) has been proposed in the literature [5]–[10]. This configuration includes m parallel SOGIs tuned to harmonic frequencies of order h_i $(i = 1, 2, \ldots, m)$.[1] In this configuration, $\hat{v}_{\alpha,h_i}$ is an estimation of the h_i-order frequency component of the input signal, $\hat{V}_{h_i}$ and $\hat{\theta}_{h_i}$ are estimations of the amplitude and phase angle of this component, and $\hat{v}_{\beta,h_i}$ is a 90°-phase-shifted version of $\hat{v}_{\alpha,h_i}$. Throughout this article, h_1 means the fundamental component.

To efficiently operate under frequency varying environments, the parallel MSOGI structure requires an estimation of the fundamental angular frequency of its single-phase input signal. This estimation may be provided in different ways. Using the frequency-locked loop (FLL) concept, which has been introduced and developed in [10]–[14], is a popular approach for this purpose. Fig. 1(b) shows a basic FLL for estimating the fundamental angular frequency and adapting parallel SOGIs to frequency changes. In this structure, λ is the FLL control gain, and $\omega_n = 2\pi 50$ rad/s is the nominal angular frequency. Note that input signals to the FLL are the error signal e and the β-axis output of the SOGI centered at the fundamental frequency, and its output is an estimation of the fundamental angular frequency. Note also that the FLL's frequency update may be obtained using the gradient descent method. Interested readers are referred to [5], [15], and [16] for more complete information. The joint operation of the MSOGI structure [see Fig. 1(a)] and the FLL [see Fig. 1(b)] is often called the MSOGI-FLL.

An alternative approach to adapt the parallel MSOGI structure is using a basic synchronous reference frame phase-locked loop (SRF-PLL), as shown in Fig. 1(c) [17]. The operation principle of this PLL is well known [18]. Therefore, it is not explained to save space. The only point to note here is that input signals of the PLL are the $\alpha\beta$-axis outputs of the SOGI$_1$, which is centered at the fundamental frequency. Therefore, $\bar{\theta}_{h_1}$ and $\bar{V}_{h_1}$ in the PLL output can be considered as a filtered version of $\hat{\theta}_{h_1}$ and $\hat{V}_{h_1}$, respectively. The joint operation of the MSOGI structure [see Fig. 1(a)] and the PLL [see Fig. 1(c)] is often called the MSOGI-PLL.

[1] A slight structural difference between MSOGI structures in the literature may be observed. The main difference often lies in the point(s) where a SOGI's center frequency (i.e., $h_i\hat{\omega}$) is applied/multiplied. It is before the input of integrators of SOGIs in Fig. 1(a).

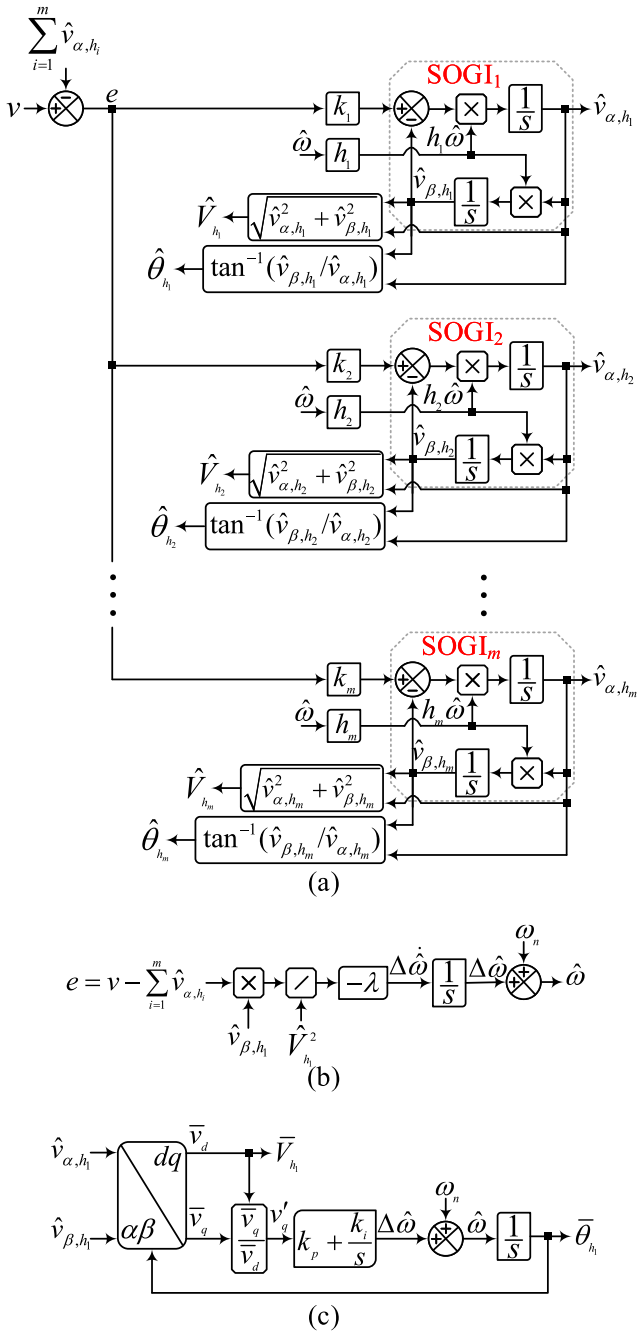

Fig. 1. (a) Parallel MSOGI configuration for the signal decomposition. (b) Basic FLL. (c) Basic PLL. Note that $h_1 = 1$.

Recently, some efforts for deriving analytic linear models and analyzing the stability of single-phase SOGI-based signal conditioning/synchronization systems have been made in the literature. For instance, in [19], an analytic linear time-periodic (LTP) model for a simple SOGI-FLL (including only one SOGI centered at the fundamental frequency) is presented, and its accuracy in predicting the stability and dynamic behavior of the SOGI-FLL is compared with that of its linear time-invariant (LTI) model. Although more accurate than the LTI one, this LTP model is not completely accurate as it neglects the amplitude estimation dynamics of the SOGI-FLL and, therefore,

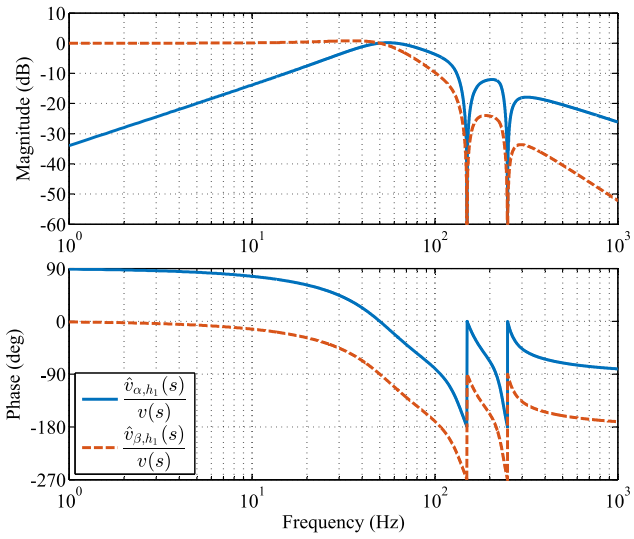

Fig. 2. Fundamental-component frequency response of an MSOGI-based signal decompoistor including three parallel SOGIs cenetred at $\hat{\omega}$, $3\hat{\omega}$, and $5\hat{\omega}$.

results in optimistic predictions about the SOGI-FLL stability. By considering the amplitude estimation dynamics, a more precise LTP model for the SOGI-FLL is presented in [20]. This model is able to accurately predict small-signal dynamics of the SOGI-FLL and determine its stability margins. In [21] and [22], some LTP models for a simple SOGI-PLL (including only one SOGI centered at the fundamental frequency) are presented. These models provide some insight into stability properties of the SOGI-PLL, and are useful for the impedance modeling and stability assessment of single-phase grid-tied converters equipped with a SOGI-PLL.

To the best of the authors' knowledge, the LTP modeling and stability assessment of MSOGI-FLL/MSOGI-PLL (including m parallel SOGIs) and their close variants have not yet been presented. Indeed, according to the above review, the available works are limited to the case of a simple SOGI-FLL/SOGI-PLL. This article aims to bridge this gap in research. To this end, LTP models of an MSOGI structure (including m parallel SOGIs), a basic FLL, and a basic PLL are obtained first. It is shown that the complete LTP model of an MSOGI-FLL and MSOGI-PLL can be easily achieved by connecting these models together. It is also shown that the open-loop harmonic transfer function (HTF) of these systems can be easily obtained using their LTP models and can be used for evaluating the effects of different factors (such as the number and center frequency of parallel SOGIs and the working condition) on their stability properties. The LTP modeling and stability assessment of some close variants of the MSOGI-FLL and MSOGI-PLL are also examined at the end of this study by obtaining their governing nonlinear differential equations and comparing them together.

II. LTP Modeling of MSOGI-Based Grid Synchronization/Monitoring Systems

A. Description

The MSOGI-based signal decompositor [see Fig. 1(a)], as mentioned before, includes a number of SOGIs centered at the fundamental and concerned harmonic frequencies. These SOGIs are connected to a common error signal, which is generated by subtracting the α-axis outputs of all SOGIs from the single-phase input signal. This configuration results in a collaborative operation between parallel SOGIs and, therefore, makes them able to adaptively extract the fundamental and concerned harmonic components of the single-phase input signal and estimate their phase angle and amplitude.

To better visualize the collaborative operation of the parallel SOGIs in Fig. 1(a), let us consider a simple case, in which there are only three parallel SOGIs centered at $\hat{\omega}$, $3\hat{\omega}$, and $5\hat{\omega}$. It is corresponding to consider $h_1 = 1$, $h_2 = 3$, and $h_3 = 5$. The control gains of these SOGIs are selected as $k_1 = 1$, $k_2 = 1/3$, and $k_3 = 1/5$. $\hat{\omega} = 2\pi 50$ rad/s is considered. The frequency response of $\frac{\hat{v}_{\alpha,h_1}(s)}{v(s)}$ and $\frac{\hat{v}_{\beta,h_1}(s)}{v(s)}$ can be observed in Fig. 2, where $\hat{v}_{\alpha,h_1}$ and $\hat{v}_{\beta,h_1}$ are the $\alpha-$ and $\beta-$axis outputs of the SOGI centered at $h_1\hat{\omega} = \hat{\omega}$. It is observed that there are two notches centered at 150 and 250 Hz in the magnitude-frequency response of $\frac{\hat{v}_{\alpha,h_1}(s)}{v(s)}$ and $\frac{\hat{v}_{\beta,h_1}(s)}{v(s)}$. These notches, which are caused by the SOGIs centered at $h_2\hat{\omega} = 3\hat{\omega}$ and $h_3\hat{\omega} = 5\hat{\omega}$, mathematically mean that the α- and β-axis outputs of the SOGI centered at the fundamental frequency are immune to (free from) the third and fifth-order harmonics of the input signal in the steady state. This feature is the result of the collaborative operation of parallel SOGIs.

B. Linear Modeling of MSOGI Structure

The aim of this part is to demonstrate the procedure for obtaining an LTP model for the MSOGI-based signal decompositor in Fig. 1(a). This procedure involves obtaining its governing nonlinear differential equations and linearizing them. Before that, some assumptions/definitions about the input and output signals of the MSOGI structure need to be made.

Note: All equations in Sections II-B, II-C, and II-D are in the time domain. To save space, the argument t is not shown in these equations.

1) Assumptions: The single-phase input signal in Fig. 1(a) is considered as

$$v = \sum_{i=1}^{m} V_{h_i} \cos(\theta_{h_i}) \tag{1}$$

where V_{h_i} and θ_{h_i} denote the amplitude and phase angle of a component of the angular frequency $h_i\omega$, respectively. ω is the fundamental angular frequency.

Considering (2) and (3), which are readily obtainable from Fig. 1(a), the output signals $\hat{v}_{\alpha,h_i}$ and $\hat{v}_{\beta,h_i}$ $(i = 1, 2, \ldots, m)$ in Fig. 1(a) can be expressed as (4) and (5)

$$\hat{V}_{h_i} = \sqrt{\hat{v}_{\alpha,h_i}^2 + \hat{v}_{\beta,h_i}^2} \tag{2}$$

$$\hat{\theta}_{h_i} = \tan^{-1}(\hat{v}_{\beta,h_i}/\hat{v}_{\alpha,h_i}) \tag{3}$$

$$\hat{v}_{\alpha,h_i} = \hat{V}_{h_i} \cos(\hat{\theta}_{h_i}) \tag{4}$$

$$\hat{v}_{\beta,h_i} = \hat{V}_{h_i} \sin(\hat{\theta}_{h_i}). \tag{5}$$

Both the actual and estimated amplitudes, phase angles, and angular frequencies are defined as a nominal value plus a small

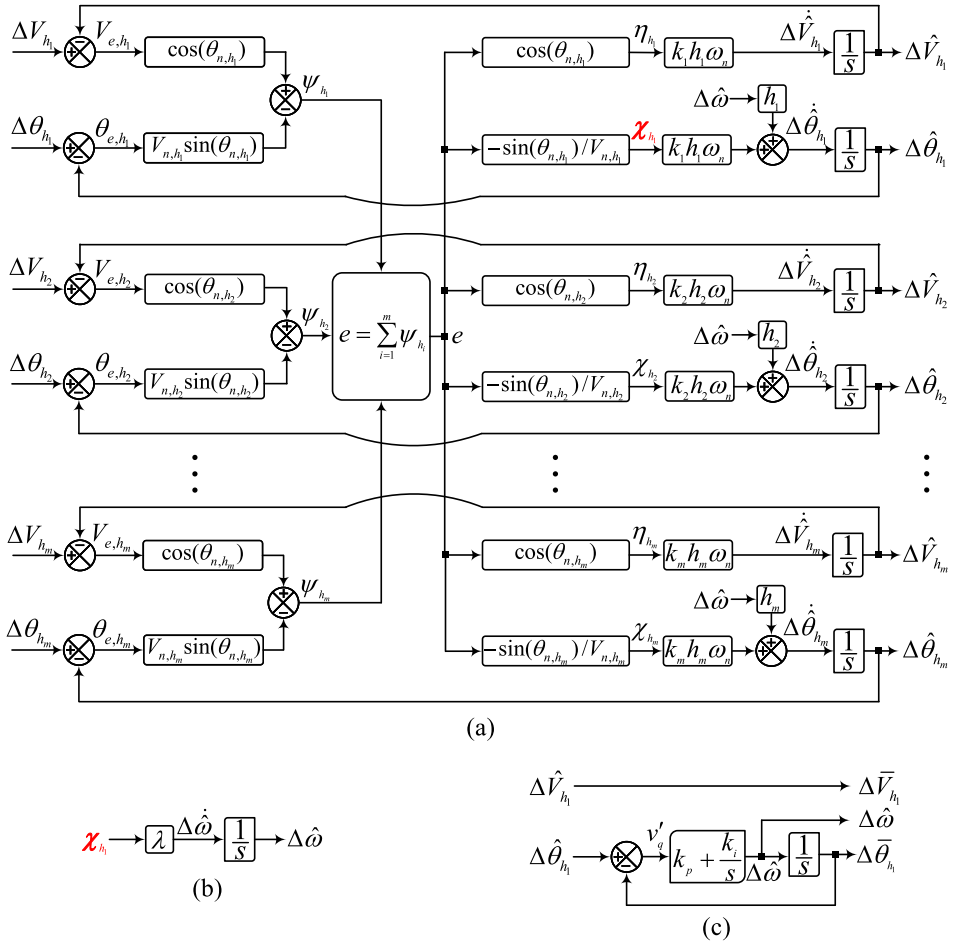

Fig. 3. Linear model of the MSOGI-based signal decompositor in Fig. 1(a). (b) Linear model of the basic FLL in Fig. 1(b). (c) Linear model of the basic PLL in Fig. 1(c). Note that $h_1 = 1$.

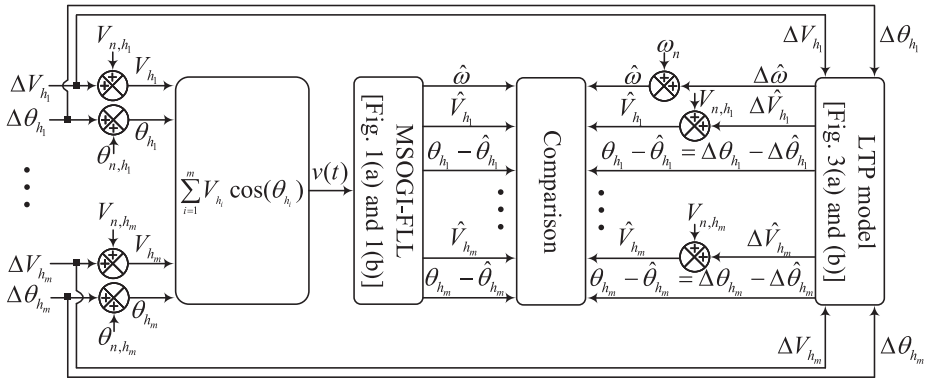

Fig. 4. Block diagram of the procedure for the model verification of the MSOGI-FLL in the time domain.

perturbation as

$$\begin{aligned} V_{h_i} &= V_{n,h_i} + \Delta V_{h_i}, \quad \hat{V}_{h_i} = V_{n,h_i} + \Delta\hat{V}_{h_i} \\ \theta_{h_i} &= \theta_{n,h_i} + \Delta\theta_{h_i}, \quad \hat{\theta}_{h_i} = \theta_{n,h_i} + \Delta\hat{\theta}_{h_i} \\ \omega &= \omega_n + \Delta\omega, \qquad \hat{\omega} = \omega_n + \Delta\hat{\omega} \end{aligned} \tag{6}$$

where $\omega_n = 2\pi 50$ rad/s and $\theta_{n,h_i} = h_i\omega_n t + \varphi_{n,h_i}$. Note that Δ and the subscript n refer to a small perturbation and a nominal value, respectively.

2) Linearization: Considering $i = 1$ in (2) and (3) and differentiating them with respect to time results in

$$\dot{\hat{V}}_{h_1} = \frac{\hat{v}_{\alpha,h_1}\dot{\hat{v}}_{\alpha,h_1} + \hat{v}_{\beta,h_1}\dot{\hat{v}}_{\beta,h_1}}{\hat{V}_{h_1}} \tag{7}$$

$$\dot{\hat{\theta}}_{h_1} = \frac{\dot{\hat{v}}_{\beta,h_1}\hat{v}_{\alpha,h_1} - \dot{\hat{v}}_{\alpha,h_1}\hat{v}_{\beta,h_1}}{\hat{V}_{h_1}^2} \tag{8}$$

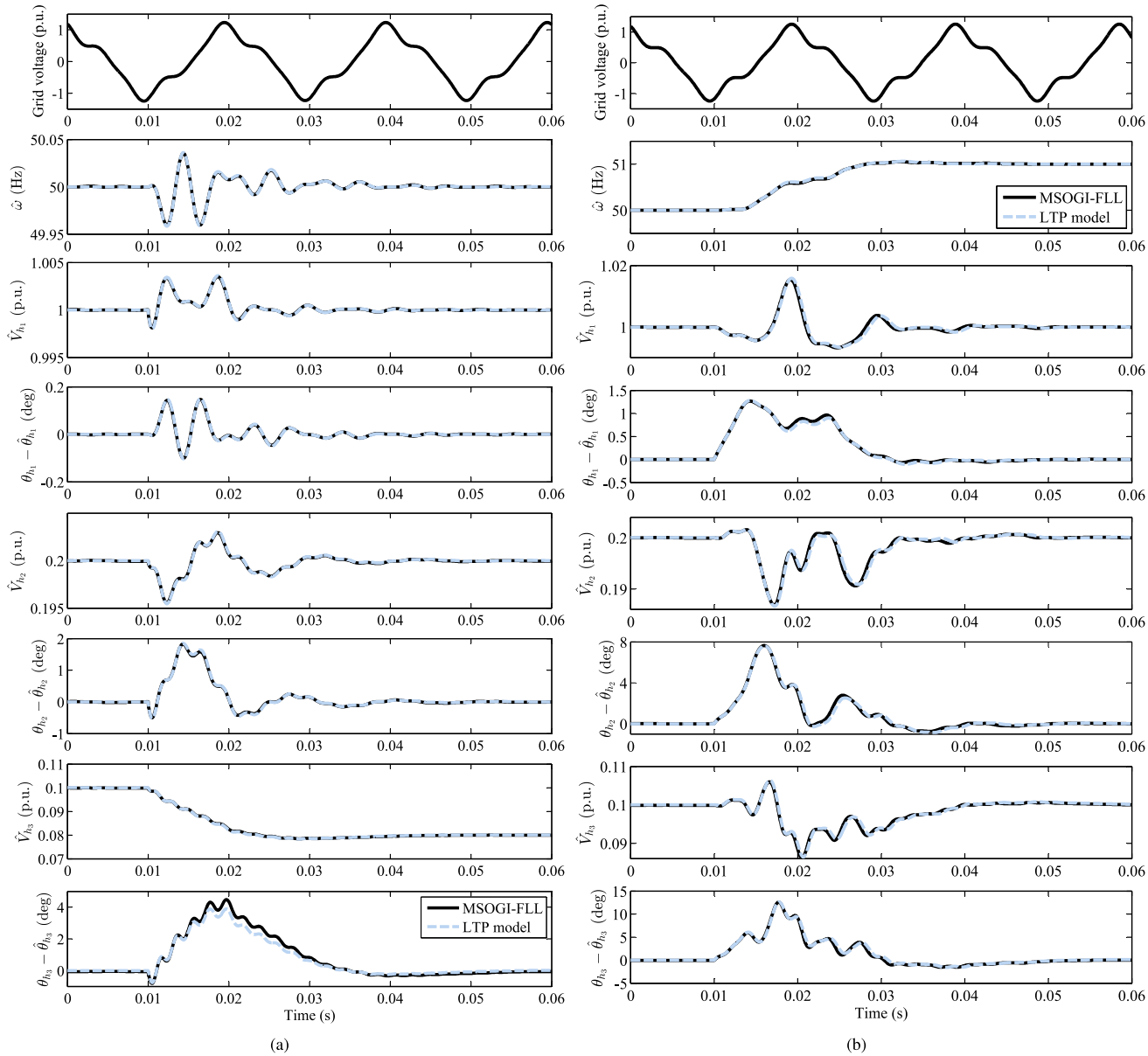

Fig. 5. Accuracy assessment of the LTP model of the MSOGI-FLL. (a) Test 1. (b) Test 2. All required parameters are summarized in Table I.

where, according to Fig. 1(a), $\dot{\hat{v}}_{\alpha,h_1}$ and $\dot{\hat{v}}_{\beta,h_1}$ are equal to

$$\dot{\hat{v}}_{\alpha,h_1} = h_1\hat{\omega}\left[k_1\left(v - \sum_{i=1}^{m}\hat{v}_{\alpha,h_i}\right) - \hat{v}_{\beta,h_1}\right] \tag{9}$$

$$\dot{\hat{v}}_{\beta,h_1} = h_1\hat{\omega}\hat{v}_{\alpha,h_1}. \tag{10}$$

Using (9) and (10), one can rewrite (7) and (8) as

$$\dot{\hat{V}}_{h_1} = k_1 h_1 \hat{\omega}\frac{\hat{v}_{\alpha,h_1}}{\hat{V}_{h_1}}\left(v - \sum_{i=1}^{m}\hat{v}_{\alpha,h_i}\right) \tag{11}$$

$$\dot{\hat{\theta}}_{h_1} = h_1\hat{\omega} - k_1 h_1\hat{\omega}\frac{\hat{\boldsymbol{v}}_{\boldsymbol{\beta},\boldsymbol{h_1}}}{\hat{\boldsymbol{V}}_{\boldsymbol{h_1}}^{\boldsymbol{2}}}\underbrace{\left(\boldsymbol{v} - \sum_{\boldsymbol{i=1}}^{\boldsymbol{m}}\hat{\boldsymbol{v}}_{\boldsymbol{\alpha},\boldsymbol{h_i}}\right)}_{\boldsymbol{e(t)}}. \tag{12}$$

The highlighted part in (12) will be explained later.

Substituting (1), (4), and (5) into (11) and (12) gives

$$\dot{\hat{V}}_{h_1} = k_1 h_1\hat{\omega}\cos(\hat{\theta}_{h_1})\sum_{i=1}^{m}\left[V_{h_i}\cos(\theta_{h_i}) - \hat{V}_{h_i}\cos(\hat{\theta}_{h_i})\right] \tag{13}$$

$$\dot{\hat{\theta}}_{h_1} = h_1\hat{\omega} - \frac{k_1 h_1\hat{\omega}}{\hat{V}_{h_1}}\sin(\hat{\theta}_{h_1})\underbrace{\sum_{i=1}^{m}\left[V_{h_i}\cos(\theta_{h_i}) - \hat{V}_{h_i}\cos(\hat{\theta}_{h_i})\right]}_{e(t)} \tag{14}$$

which are a set of nonlinear differential equations governing the dynamics of estimating $\hat{V}_{h_1}$ and $\hat{\theta}_{h_1}$ in Fig. 1(a).

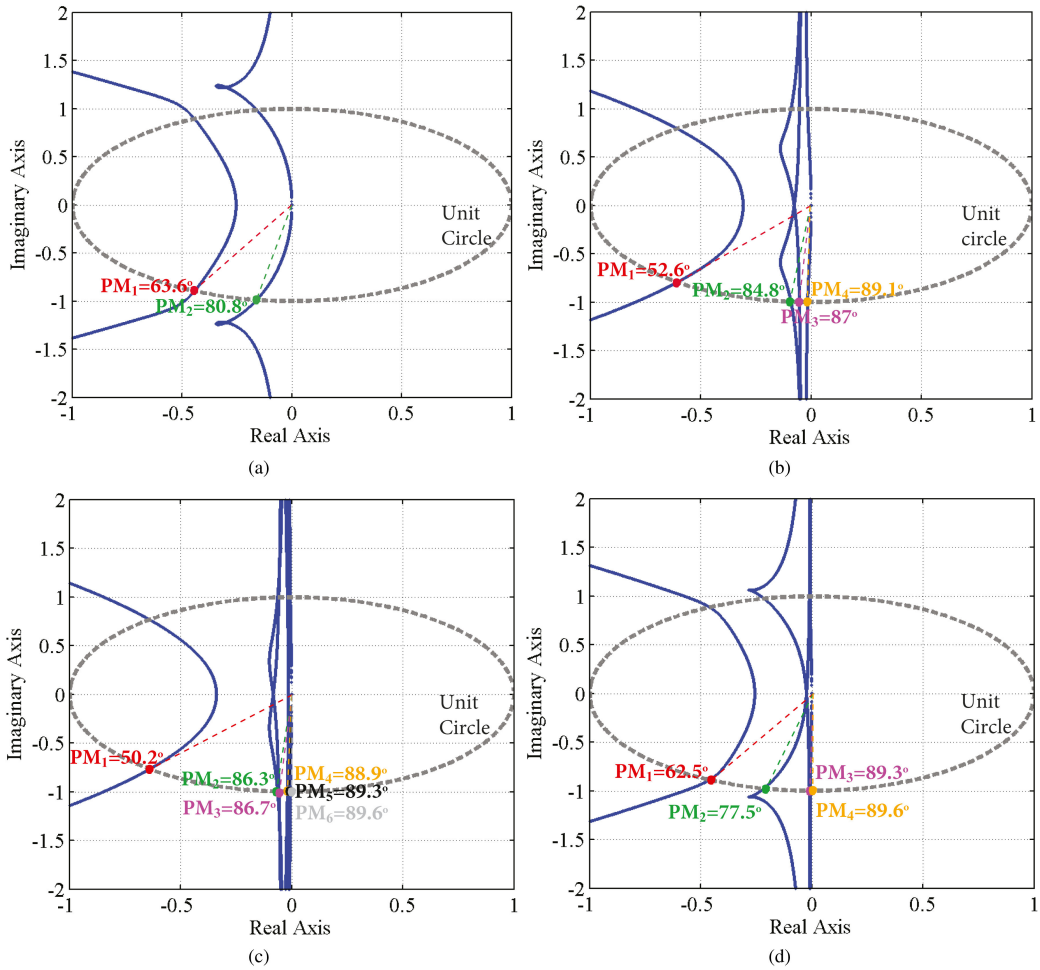

Fig. 6. Open-loop LTP eigenloci. (a) Simple SOGI-FLL (see Case 1 in Table II). (b) DSOGI-FLL (see Case 2 in Table II). (c) MSOGI-FLL (see Case 3 in Table II). (d) DSOGI-FLL (see Case 4 in Table II).

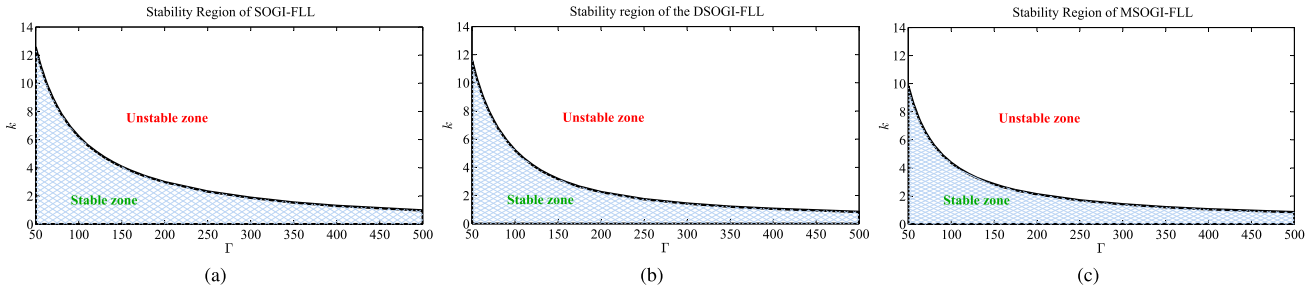

Fig. 7. Stability region. (a) SOGI-FLL (see Case 1 in Table II). (b) DSOGI-FLL (see Case 2 in Table II). (c) MSOGI-FLL (see Case 3 in Table II). Note that obtaining these stability regions is based on considering $h_i k_i = k$ $(i = 1, \ldots, m)$ and $\Gamma = \lambda/(k\omega_n)$.

Both (13) and (14) have a common term $e(t)$, which its linearization is shown in the Appendix [see (56)]. Using (56) in the Appendix and also the definitions made in (6), the above equations can be linearized as

$$\Delta\dot{\hat{V}}_{h_1} \approx k_1 h_1 \omega_n \cos(\theta_{n,h_1}) \sum_{i=1}^{m} \psi_{h_i} \tag{15}$$

$$\Delta\dot{\hat{\theta}}_{h_1} \approx h_1 \Delta\hat{\omega} - k_1 h_1 \omega_n \frac{\sin(\theta_{n,h_1})}{V_{n,h_1}} \sum_{i=1}^{m} \psi_{h_i}. \tag{16}$$

These equations, which are a set of LTP differential equations, describe the linearized dynamics of the MSOGI-based signal decompositor [see Fig. 1(a)] in estimating $\hat{V}_{h_1}$ and $\hat{\theta}_{h_1}$.

Following a similar procedure as above, one can obtain (17) and (18), which describe the linearized dynamics of the MSOGI-based signal decompositor [see Fig. 1(a)] in estimating $\hat{V}_{h_m}$ and

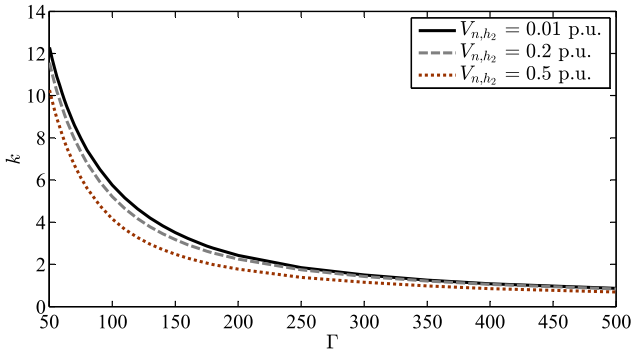

Fig. 8. Changing the stability region of the DSOGI-FLL (see Case 2 in Table II) as a function of V_{n,h_2}. Note that the area below each curve is the DSOGI-FLL's stability region for its corresponding V_{n,h_2}.

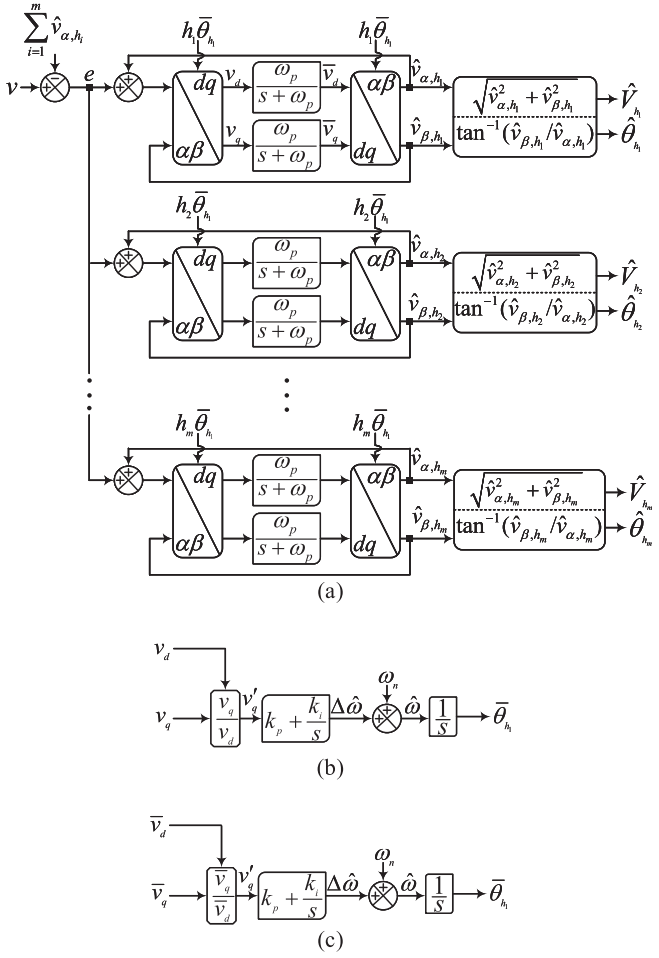

Fig. 9. (a) Multiple IPT-based signal decomposition. (b) and (c) Basic PLLs. Note that $h_1 = 1$.

$\hat{\theta}_{h_m}$

$$\Delta\dot{\hat{V}}_{h_m} \approx k_m h_m \omega_n \cos(\theta_{n,h_m}) \sum_{i=1}^{m} \psi_{h_i} \tag{17}$$

$$\Delta\dot{\hat{\theta}}_{h_m} \approx h_m \Delta\hat{\omega} - k_m h_m \omega_n \frac{\sin(\theta_{n,h_m})}{V_{n,h_m}} \sum_{i=1}^{m} \psi_{h_i}. \tag{18}$$

Using (15)–(18), the LTP model of the MSOGI-based signal decompositor can be obtained as shown in Fig. 3(a).

C. Linear Modeling of FLL

The MSOGI-based signal decomposition algorithm in Fig. 1(a), as mentioned before, requires an estimation of the fundamental angular frequency for adapting its SOGIs to frequency changes. It was mentioned that a popular way to provide this frequency estimation is using an FLL, as shown in Fig. 1(b). The joint operation of this FLL and the MSOGI structure in Fig. 1(a) was named the MSOGI-FLL. In what follows, the linear model of this basic FLL will be obtained. Coupling the resulting model with that of the MSOGI-based signal decompoistor [see Fig. 3(a)] gives the complete LTP model of the MSOGI-FLL.

From Fig. 1(b), the nonlinear differential equation governing the dynamics of the FLL in estimating the fundamental angular frequency can be obtained as

$$\Delta\dot{\hat{\omega}} = -\lambda \frac{\hat{\boldsymbol{v}}_{\boldsymbol{\beta},\boldsymbol{h_1}}}{\hat{\boldsymbol{V}}_{\boldsymbol{h_1}}^{\boldsymbol{2}}} \left(\boldsymbol{v} - \sum_{\boldsymbol{i=1}}^{\boldsymbol{m}} \hat{\boldsymbol{v}}_{\boldsymbol{\alpha},\boldsymbol{h_i}} \right). \tag{19}$$

The above equation and (12) have a common nonlinear term highlighted in bold. Considering (16), which is the result of the lineraization of (12), (19) can be linearized as

$$\Delta\dot{\hat{\omega}} \approx \underbrace{-\left[\frac{\sin(\theta_{n,h_1})}{V_{n,h_1}} \sum_{i=1}^{m} \psi_{h_i} \right]}_{\chi_{h_1}} \lambda. \tag{20}$$

Based on the above equation, the linearized model of the FLL can be obtained as depicted in Fig. 3(b). Note that the signal χ_{h_1} is highlighted in Fig. 3(a).

D. Linear Modeling of PLL

As pointed out before, an alternative way for providing an estimation of the fundamental angular frequency and adapting SOGIs in Fig. 1(a) to frequency changes is using a basic PLL, as shown in Fig. 1(c). Note that the α- and β-axis inputs of this PLL are the α- and β-axis outputs of the first SOGI in Fig. 1(a), i.e., the SOGI centered at $h_1\hat{\omega}$. Recall that $h_1 = 1$. The joint operation of the MSOGI-based signal decompositor in Fig. 1(a) and the basic PLL in Fig. 1(c) is often briefly called the MSOGI-PLL.

In what follows, the linear model of the basic PLL in Fig. 1(c) will be obtained. Coupling this model with that of the MSOGI-based signal decompoistor [see Fig. 3(a)] gives the complete LTP model of the MSOGI-PLL.

Considering (4) and (5), which mathematically describe the $\alpha\beta$-axis outputs of the ith SOGI in Fig. 1(a), and the Park transformation in (21), the signals v_d and v_q in Fig. 1(c) can be obtained as (22)

$$T_{\alpha\beta\to dq} = \begin{bmatrix} \cos(\bar{\theta}_{h_1}) & \sin(\bar{\theta}_{h_1}) \\ -\sin(\bar{\theta}_{h_1}) & \cos(\bar{\theta}_{h_1}) \end{bmatrix} \tag{21}$$

$$\begin{bmatrix} \bar{v}_d \\ \bar{v}_q \end{bmatrix} = T_{\alpha\beta\to dq} \begin{bmatrix} \hat{v}_{\alpha,h_1} \\ \hat{v}_{\beta,h_1} \end{bmatrix} = \begin{bmatrix} \hat{V}_{h_1} \cos(\hat{\theta}_{h_1} - \bar{\theta}_{h_1}) \\ \hat{V}_{h_1} \sin(\hat{\theta}_{h_1} - \bar{\theta}_{h_1}) \end{bmatrix}. \tag{22}$$

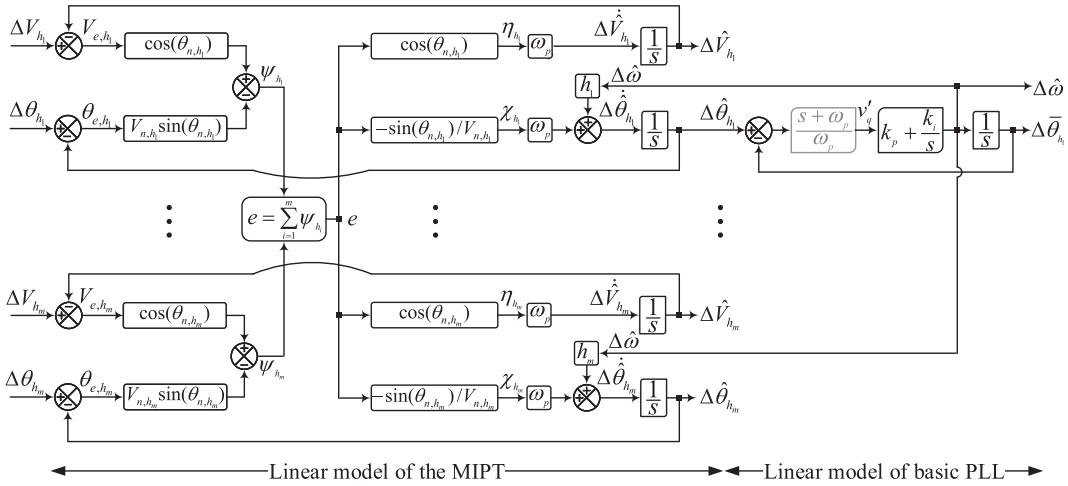

Fig. 10. LTP model of the MIPT-PLL. Note that this LTP model is corresponding to the MIPT in Fig. 9(a) and the basic PLL in Fig. 9(b). Note also that the block with the transfer function $\frac{s+\omega_p}{\omega_p}$ in the model should be removed if the basic PLL in Fig. 9(c) is considered.

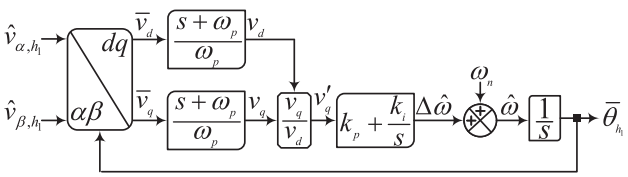

Fig. 11. Alternative representation of the basic PLL in Fig. 9(b).

Considering the definitions already made in (6) and also defining $\bar{\theta}_{h_1} = \theta_{n,h_1} + \Delta\bar{\theta}_{h_1}$ and $\bar{V}_{h_1} = V_{n,h_1} + \Delta\bar{V}_{h_1}$, (22) can be linearized as

$$\bar{v}_d = \left(V_{n,h_1} + \Delta\hat{V}_{h_1}\right)\overbrace{\cos(\Delta\hat{\theta}_{h_1} - \Delta\bar{\theta}_{h_1})}^{\approx 1} \approx V_{n,h_1} + \Delta\hat{V}_{h_1} \tag{23}$$

$$\bar{v}_q = \left(V_{n,h_1} + \Delta\hat{V}_{h_1}\right)\overbrace{\sin(\Delta\hat{\theta}_{h_1} - \Delta\bar{\theta}_{h_1})}^{\approx(\Delta\hat{\theta}_{h_1} - \Delta\bar{\theta}_{h_1})} \approx V_{n,h_1}(\Delta\hat{\theta}_{h_1} - \Delta\bar{\theta}_{h_1}). \tag{24}$$

Using (23), (24), and the basic PLL structure in Fig. 1(c), one can obtain

$$\bar{V}_{h_1} = \bar{v}_d \Rightarrow \Delta\bar{V}_{h_1} \approx \Delta\hat{V}_{h_1} \tag{25}$$

$$v'_q = \frac{\bar{v}_q}{\bar{v}_d} \approx \frac{V_{n,h_1}(\Delta\hat{\theta}_{h_1} - \Delta\bar{\theta}_{h_1})}{V_{n,h_1} + \Delta\hat{V}_{h_1}} \approx (\Delta\hat{\theta}_{h_1} - \Delta\bar{\theta}_{h_1}). \tag{26}$$

Considering the above equations, obtaining the linear model shown in Fig. 3(c) for the basic PLL in Fig. 1(c) is quite straightforward.

E. Model Verification

As mentioned before, connecting the models shown in Fig. 3(a) and (b) gives the complete LTP model of the MSOGI-FLL. In this section, the accuracy of this LTP model will be investigated in MATLAB/Simulink. The block diagram shown in Fig. 4 indicates how the model verification is carried out, and Table I summarizes the selected control parameters for the MSOGI-FLL and also the nominal values of different components of its input signal. The control parameters of the MSOGI-FLL are taken from [5].

Both the MSOGI-FLL and its LTP model are discretized with a sampling frequency of 20 kHz. The SOGIs of the MSOGI-FLL are discretized using the third-order Adams–Bashforth method [17]. The rest of the integrators in both the MSOGI-FLL and its LTP model are discretized using backward and forward Euler methods.

The following tests are considered for the model verification.

1) *Test 1*: The magnitude of the harmonic of order $h_3 = 5$ suddenly changes from its nominal value, i.e., $V_{h_3} = V_{n,h_3} = 0.1$ p.u., to $V_{h_3} = 0.08$ p.u. at $t = 0.01$ s.
2) *Test 2*: The fundamental angular frequency of the single-phase input signal is suddenly changes from its nominal value, i.e., $\omega = \omega_n = 2\pi 50$ rad/s, to $\omega = 2\pi 51$ rad/s at $t = 0.01$ s.

The results of the above tests are shown in Fig. 5. It is observed that the LTP model demonstrates good accuracy in predicting the MSOGI-FLL dynamics. The model verification of the MSOGI-PLL may also be carried out in a similar manner as above.

Here, it needs to be emphasized that the condition of the model verification may considerably affect the observations made about the model accuracy. Generally speaking, the more consistent the condition of the model verification is with the assumptions behind obtaining the LTP model, the higher the model accuracy will be. For instance, as shown in (6), each parameter is defined as a nominal value plus a small perturbation. It implies that applying a large perturbation during the model

TABLE I
SELECTED PARAMETERS FOR THE MODEL VERIFICATION OF THE MSOGI-FLL

MSOGI-FLL				Single-phase input signal		
Number of SOGIs	Concerned harmonics	SOGI gains	FLL gain	Nominal frequency	Nominal amplitudes	Nominal phase angles
$m = 3$	$h_1 = 1$	$k_1 = k/h_1 = \sqrt{2}$	$\lambda = 49348$ rad/s^2	$\omega_n = 2\pi 50$ rad/s	$V_{n,h_1} = 1$ p.u.	$\theta_{n,h_1} = h_1\omega_n t + 0$
	$h_2 = 3$	$k_2 = k/h_2 = \sqrt{2}/3$			$V_{n,h_2} = 0.2$ p.u.	$\theta_{n,h_2} = h_2\omega_n t + \pi/3$
	$h_3 = 5$	$k_3 = k/h_3 = \sqrt{2}/5$			$V_{n,h_3} = 0.1$ p.u.	$\theta_{n,h_3} = h_3\omega_n t + \pi/6$

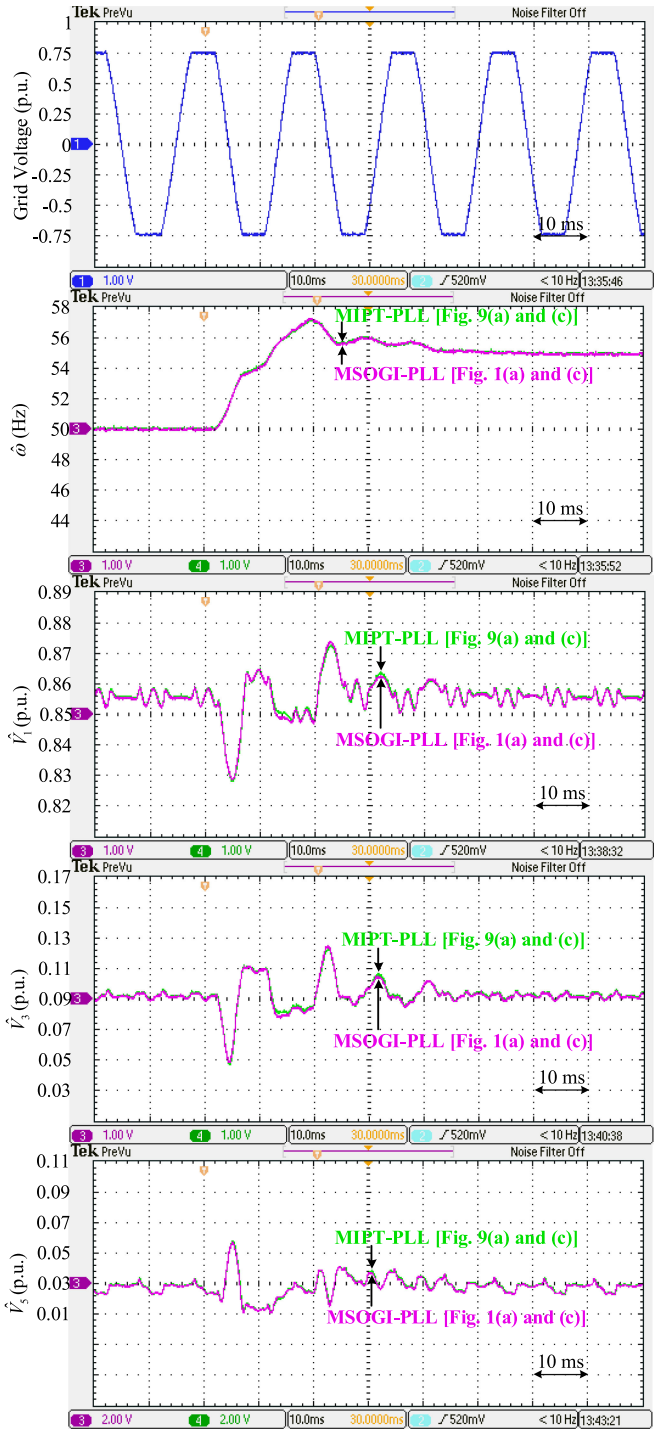

Fig. 12. Experimental comparison between the MSOGI-PLL and MIPT-PLL under a +5-Hz frequency jump in a harmonic-rich grid condition.

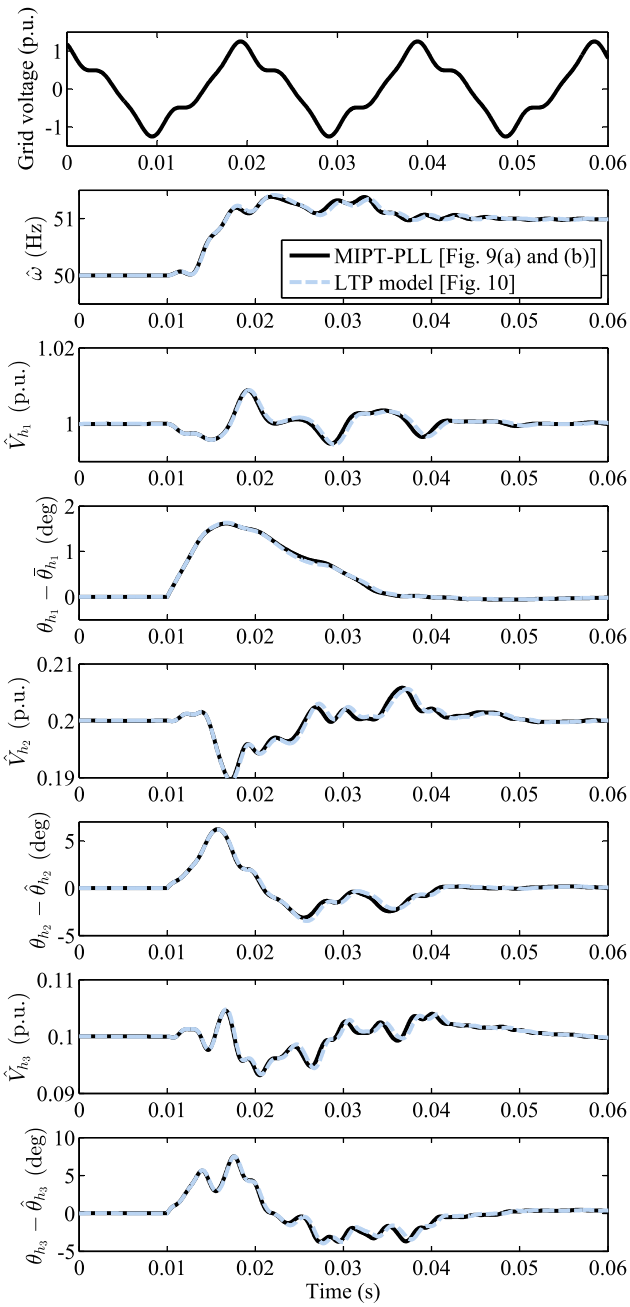

Fig. 13. Accuracy assessment of the LTP model of the MIPT-PLL in response to a +1-Hz frequency jump (see Test 2 in Section II-E).

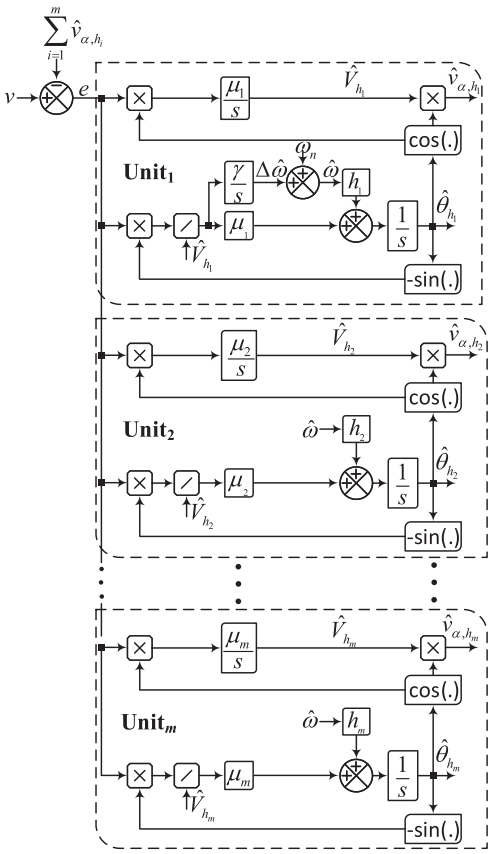

Fig. 14. MEPLL system. Note that $h_1 = 1$.

verification contradicts this assumption and, therefore, reduces the model accuracy. Another instance is the sampling frequency. The LTP modeling of the MSOGI-FLL/MSOGI-PLL was based on their continuous-time presentations in Fig. 1. It implies that the implementation at a high sampling frequency has been assumed. Therefore, the model accuracy will be reduced if a low sampling frequency in the model verification is considered. This is particularly true if the MSOGI-FLL/MSOGI-PLL contains a SOGI centered at high-order harmonic frequencies.

III. Stability Analysis

A. Open-Loop Harmonic Transfer Function

The main aim of this section is to conduct a stability analysis on the MSOGI-FLL. Obtaining the open-loop HTF of the MSOGI-FLL makes achieving this objective easier. To make the understanding of this procedure more straightforward, some examples are provided first. Note that the stability analysis of the MSOGI-PLL may also be carried out in a similar manner.

1) Example 1 - Multiplication by a Trigonometric Function: In the LTP model of the MSOGI-FLL, which is obtained by connecting Fig. 3(a) and (b) together, there are several multiplications with trigonometric functions. Therefore, for obtaining the open-loop HTF of the MSOGI-FLL, it is important to learn how the HTF of such multiplications should be obtained. The key point to keep in mind here is that all trigonometric functions

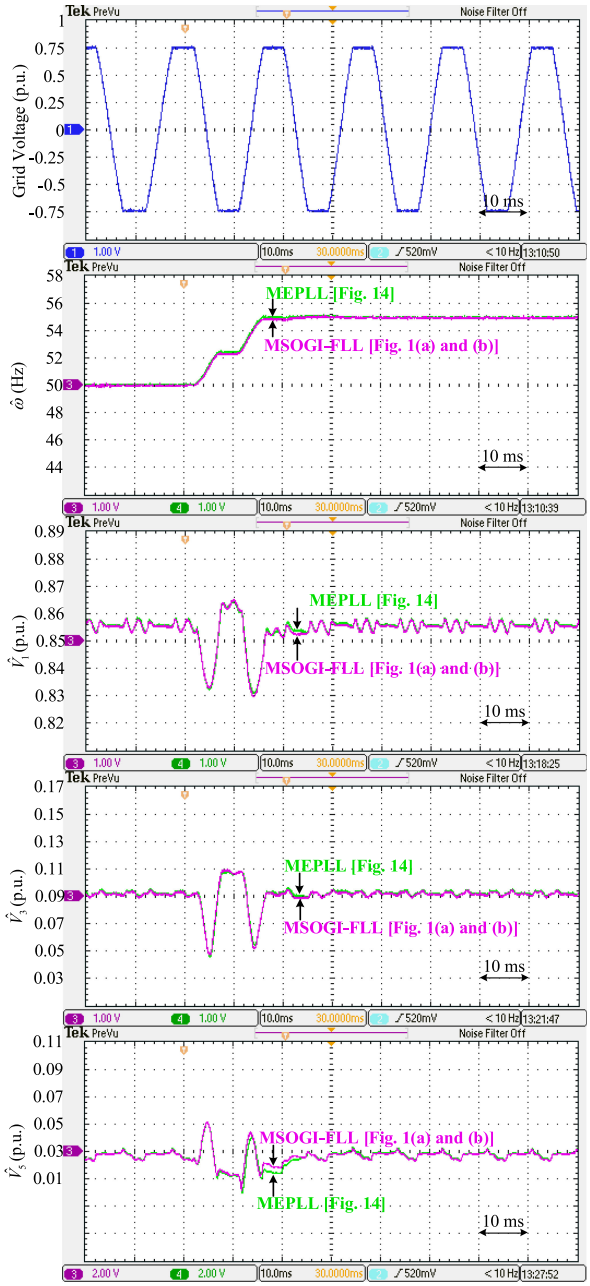

Fig. 15. Experimental comparison between the MSOGI-FLL and MEPLL system. The control parameters of the MSOGI-FLL, the number of its SOGIs, and their center frequencies can be found in Table I. The control parameters of the MEPLL are selected so that its small-signal equivalence with the MSOGI-FLL is satisfied.

in the LTP model of the MSOGI-FLL are harmonics of the fundamental component, i.e., the component of the angular frequency $h_1\omega_n$.

First, the multiplication by a fundamental-frequency trigonometric term [see (27)] is considered

$$y(t) = \cos(\theta_{n,h_1})u(t) = \cos(h_1\omega_n t + \varphi_{n,h_1})u(t). \quad (27)$$

Recall that $h_1 = 1$.

If we replace the cosine term in (27) by its equivalent expression in terms of exponential functions, i.e., $\cos(h_1\omega_n t +$

$\varphi_{n,h_1}) = \frac{e^{j\varphi_{n,h_1}} e^{jh_1\omega_n t} + e^{-j\varphi_{n,h_1}} e^{-jh_1\omega_n t}}{2}$, this equation can be rewritten in the Laplace domain as

$$y(s) = \frac{1}{2} e^{j\varphi_{n,h_1}} u(s - jh_1\omega_n) + \frac{1}{2} e^{-j\varphi_{n,h_1}} u(s + jh_1\omega_n). \tag{28}$$

Using the above equation and its frequency-shifted versions, one can obtain (29) at the bottom of this page. The matrix $\boldsymbol{A}^{\mathbf{htf}}_{\mathbf{cos},\boldsymbol{h_1}}$ in (29) is the HTF of the multiplication by the trigonometric term $\cos(\theta_{n,h_1})$.

Now, the multiplication by a harmonic-frequency trigonometric term [see (30)] is considered

$$\begin{aligned} y(t) &= \cos(\theta_{n,h_m}) u(t) = \cos(h_m\omega_n t + \varphi_{n,h_m}) u(t) \\ &= \frac{e^{j\varphi_{n,h_m}} e^{jh_m\omega_n t} + e^{-j\varphi_{n,h_m}} e^{-jh_m\omega_n t}}{2} u(t). \end{aligned} \tag{30}$$

The important point in obtaining the HTF representation of (30) is that the resulting HTF should have the same dimension as (29).

For the sake of simplicity and brevity, it is assumed that $h_m = 2h_1$. By considering this assumption, taking the Laplace transform of (30) results in

$$y(s) = \frac{1}{2} e^{j\varphi_{n,h_m}} u(s - j2h_1\omega_n) + \frac{1}{2} e^{-j\varphi_{n,h_m}} u(s + j2h_1\omega_n). \tag{31}$$

Using the above equation and its frequency-shifted versions, and considering the fact that the resulting HTF should have the same dimension as (29), one can obtain (32) at the bottom of the next page. The matrix $\boldsymbol{A}^{\mathbf{htf}}_{\mathbf{cos},\boldsymbol{h_m}}$ in (32) is the HTF of the multiplication by the trigonometric term $\cos(\theta_{n,h_m})$

2) Example 2 - Linear Time-Invariant (LTI) Systems: An LTI system is a special case of an LTP system, where there is no coupling between its frequency components. Therefore, we should be able to represent it in the HTF form.

For instance, assume that $y(s)=G(s)u(s)$, where $G(s)$ is an ordinary transfer function. In this case, the HTF-form representation of this LTI system is $\boldsymbol{y}^{\mathbf{htf}}(s)=\boldsymbol{G}^{\mathbf{htf}}(s)\boldsymbol{u}^{\mathbf{htf}}(s)$, where $\boldsymbol{G}^{\mathbf{htf}}(s)=\mathrm{diag}(\cdots, G(s-jh_1\omega_n), G(s), G(s+jh_1\omega_n), \cdots)$ [23]. Note that the resulting HTF should have the same dimension as (29).

3) Obtaining Open-Loop HTF: Using the previous examples, one can obtain (33)–(35) at the bottom of the next page from the LTP model of the MSOGI-FLL [see Fig. 3(a) and (b)], where $G_{\mathrm{int}}(s) = \frac{1}{s}$ and $\boldsymbol{G}^{\mathbf{htf}}_{\mathbf{int}}(s) = \mathrm{diag}(\cdots, G_{\mathrm{int}}(s - jh_1\omega_n), G_{\mathrm{int}}(s), G_{\mathrm{int}}(s + jh_1\omega_n), \cdots)$. Based on these equations, the open-loop HTF of the MSOGI-FLL can be readily obtained as

$$\begin{bmatrix} \boldsymbol{\Delta}\hat{\boldsymbol{V}}^{\mathbf{htf}}_{\boldsymbol{h_1}} \\ \boldsymbol{\Delta}\hat{\boldsymbol{\theta}}^{\mathbf{htf}}_{\boldsymbol{h_1}} \\ \boldsymbol{\Delta}\hat{\boldsymbol{V}}^{\mathbf{htf}}_{\boldsymbol{h_2}} \\ \boldsymbol{\Delta}\hat{\boldsymbol{\theta}}^{\mathbf{htf}}_{\boldsymbol{h_2}} \\ \vdots \\ \boldsymbol{\Delta}\hat{\boldsymbol{V}}^{\mathbf{htf}}_{\boldsymbol{h_m}} \\ \boldsymbol{\Delta}\hat{\boldsymbol{\theta}}^{\mathbf{htf}}_{\boldsymbol{h_m}} \end{bmatrix} = \underbrace{\boldsymbol{G}^{\mathbf{htf}}_{\boldsymbol{a}} \boldsymbol{G}^{\mathbf{htf}}_{\boldsymbol{b}} \boldsymbol{G}^{\mathbf{htf}}_{\boldsymbol{c}}}_{\boldsymbol{G}^{\mathbf{htf}}_{\boldsymbol{ol}}} \begin{bmatrix} \boldsymbol{V}^{\mathbf{htf}}_{\boldsymbol{e},\boldsymbol{h_1}} \\ \boldsymbol{\theta}^{\mathbf{htf}}_{\boldsymbol{e},\boldsymbol{h_1}} \\ \boldsymbol{V}^{\mathbf{htf}}_{\boldsymbol{e},\boldsymbol{h_2}} \\ \boldsymbol{\theta}^{\mathbf{htf}}_{\boldsymbol{e},\boldsymbol{h_2}} \\ \vdots \\ \boldsymbol{V}^{\mathbf{htf}}_{\boldsymbol{e},\boldsymbol{h_m}} \\ \boldsymbol{\theta}^{\mathbf{htf}}_{\boldsymbol{e},\boldsymbol{h_m}} \end{bmatrix}. \tag{36}$$

In a similar manner, the open-loop HTF of the MSOGI-PLL may be obtained.

B. Stability Margin

In this part, we are going to investigate how different factors affect the stability margin of the MSOGI-FLL. To this end, a number of case studies are considered (see Table II). In each case, the open-loop eigenloci of the MSOGI-FLL are obtained and investigated using its open-loop HTF [see (36)].

First, it can be interesting to see stability margins of a simple SOGI-FLL, which includes a single SOGI centered at the fundamental frequency and an FLL for adapting this SOGI to frequency changes (see Case 1 in Table II). Fig. 6(a) shows the open-loop eigenloci of the SOGI-FLL. Note that the SOGI-FLL has two open-loop eigenvalue curves, which intersect the lower half of the unit circle and also the real axis at two points. It means that it has two eigenvalue phase margins (PMs) and two eigenvalue gain margins (GMs). The PMs of the SOGI-FLL are highlighted in Fig. 6(a), and both its PMs and GMs are summarized in Table III.

Now, a dual-SOGI-FLL (DSOGI-FLL), which includes two parallel SOGIs centered at the fundamental and third-order harmonic frequencies, is considered (see Case 2 in Table II). The open-loop eigenloci of this DSOGI-FLL can be observed in Fig. 6(b). A difference compared with Case 1 (i.e., the simple

$$\underbrace{\begin{bmatrix} \vdots \\ y(s-j2h_1\omega_n) \\ y(s-jh_1\omega_n) \\ y(s) \\ y(s+jh_1\omega_n) \\ y(s+j2h_1\omega_n) \\ \vdots \end{bmatrix}}_{\boldsymbol{y}^{\mathbf{htf}}} = \frac{1}{2} \underbrace{\begin{bmatrix} \ddots & \ddots & \ddots & \ddots & \ddots & & \\ \ddots & 0 & e^{-j\varphi_{n,h_1}} & 0 & 0 & 0 & \\ \ddots & e^{j\varphi_{n,h_1}} & 0 & e^{-j\varphi_{n,h_1}} & 0 & 0 & \ddots \\ \ddots & 0 & e^{j\varphi_{n,h_1}} & 0 & e^{-j\varphi_{n,h_1}} & 0 & \ddots \\ \ddots & 0 & 0 & e^{j\varphi_{n,h_1}} & 0 & e^{-j\varphi_{n,h_1}} & \ddots \\ & 0 & 0 & 0 & e^{j\varphi_{n,h_1}} & 0 & \ddots \\ & & \ddots & \ddots & \ddots & \ddots & \ddots \end{bmatrix}}_{\boldsymbol{A}^{\mathbf{htf}}_{\mathbf{cos},\boldsymbol{h_1}}} \underbrace{\begin{bmatrix} \vdots \\ u(s-j2h_1\omega_n) \\ u(s-jh_1\omega_n) \\ u(s) \\ u(s+jh_1\omega_n) \\ u(s+j2h_1\omega_n) \\ \vdots \end{bmatrix}}_{\boldsymbol{u}^{\mathbf{htf}}} \tag{29}$$

SOGI-FLL) is that the DSOGI-FLL has four eigenvalue curves and, therefore, four eigenvalue PMs and GMs (see Table III). This difference makes the comparison of their stability properties a bit difficult. However, roughly speaking, it can be observed that the simple SOGI-FLL (Case 1) has more decent stability margins compared to the DSOGI-FLL (Case 2).[2]

In this stage, it can be interesting to see if the number of parallel SOGIs affects stability properties. To this end, an MSOGI-FLL including three SOGIs centered at fundamental, third, and fifth-harmonic frequencies is considered (see Case 3 in Table II), and its stability margins are obtained and compared to Case 2. The open-loop eigenloci of this MSOGI-FLL can be observed in Fig. 6(c), and its stability margins are summarized in Table III. Note that the MSOGI-FLL (Case 3) has six eigenvalue PMs and GMs, while the DSOGI-FLL (Case 2) has four eigenvalue PMs and GMs. This difference makes the comparison of their stability properties a bit difficult. However, roughly speaking, a slight reduction in stability margins of MSOGI-FLL (Case 3) compared to the DSOGI-FLL (Case 2) is observable. This

[2]This conclusion is mainly based on comparing the minimum PM and GM of these systems together.

$$\underbrace{\begin{bmatrix}\vdots\\ y(s-j2h_1\omega_n)\\ y(s-jh_1\omega_n)\\ y(s)\\ y(s+jh_1\omega_n)\\ y(s+j2h_1\omega_n)\\ \vdots\end{bmatrix}}_{\boldsymbol{y}^{\mathbf{htf}}} = \underbrace{\frac{1}{2}\begin{bmatrix}\ddots & \ddots & \ddots & \ddots & \ddots & \\ \ddots & 0 & 0 & e^{-j\varphi_{n,h_m}} & 0 & 0 & \\ \ddots & 0 & 0 & 0 & e^{-j\varphi_{n,h_m}} & 0 & \ddots \\ \ddots & e^{j\varphi_{n,h_m}} & 0 & 0 & 0 & e^{-j\varphi_{n,h_m}} & \ddots \\ \ddots & 0 & e^{j\varphi_{n,h_m}} & 0 & 0 & 0 & \ddots \\ & 0 & 0 & e^{j\varphi_{n,h_m}} & 0 & 0 & \ddots \\ & & \ddots & \ddots & \ddots & \ddots & \ddots\end{bmatrix}}_{\boldsymbol{A}^{\mathbf{htf}}_{\mathbf{cos},\boldsymbol{h_m}}} \underbrace{\begin{bmatrix}\vdots\\ u(s-j2h_1\omega_n)\\ u(s-jh_1\omega_n)\\ u(s)\\ u(s+jh_1\omega_n)\\ u(s+j2h_1\omega_n)\\ \vdots\end{bmatrix}}_{\boldsymbol{u}^{\mathbf{htf}}} \tag{32}$$

$$\begin{bmatrix}\boldsymbol{\psi}^{\mathbf{htf}}_{\boldsymbol{h_1}}\\ \boldsymbol{\psi}^{\mathbf{htf}}_{\boldsymbol{h_2}}\\ \vdots\\ \boldsymbol{\psi}^{\mathbf{htf}}_{\boldsymbol{h_m}}\end{bmatrix} = \underbrace{\begin{bmatrix}\boldsymbol{A}^{\mathbf{htf}}_{\mathbf{cos},\boldsymbol{h_1}} & -V_{n,h_1}\boldsymbol{A}^{\mathbf{htf}}_{\mathbf{sin},\boldsymbol{h_1}} & \boldsymbol{0} & \boldsymbol{0} & \cdots & \boldsymbol{0} & \boldsymbol{0}\\ \boldsymbol{0} & \boldsymbol{0} & \boldsymbol{A}^{\mathbf{htf}}_{\mathbf{cos},\boldsymbol{h_2}} & -V_{n,h_2}\boldsymbol{A}^{\mathbf{htf}}_{\mathbf{sin},\boldsymbol{h_2}} & \cdots & \boldsymbol{0} & \boldsymbol{0}\\ \vdots & \vdots & \vdots & \vdots & \ddots & \vdots & \vdots\\ \boldsymbol{0} & \boldsymbol{0} & \boldsymbol{0} & \boldsymbol{0} & \cdots & \boldsymbol{A}^{\mathbf{htf}}_{\mathbf{cos},\boldsymbol{h_m}} & -V_{n,h_m}\boldsymbol{A}^{\mathbf{htf}}_{\mathbf{sin},\boldsymbol{h_m}}\end{bmatrix}}_{\boldsymbol{G}^{\mathbf{htf}}_{\boldsymbol{c}}} \begin{bmatrix}\boldsymbol{V}^{\mathbf{htf}}_{\boldsymbol{e},\boldsymbol{h_1}}\\ \boldsymbol{\theta}^{\mathbf{htf}}_{\boldsymbol{e},\boldsymbol{h_1}}\\ \boldsymbol{V}^{\mathbf{htf}}_{\boldsymbol{e},\boldsymbol{h_2}}\\ \boldsymbol{\theta}^{\mathbf{htf}}_{\boldsymbol{e},\boldsymbol{h_2}}\\ \vdots\\ \boldsymbol{V}^{\mathbf{htf}}_{\boldsymbol{e},\boldsymbol{h_m}}\\ \boldsymbol{\theta}^{\mathbf{htf}}_{\boldsymbol{e},\boldsymbol{h_m}}\end{bmatrix} \tag{33}$$

$$\begin{bmatrix}\boldsymbol{\eta}^{\mathbf{htf}}_{\boldsymbol{h_1}}\\ \boldsymbol{\chi}^{\mathbf{htf}}_{\boldsymbol{h_1}}\\ \boldsymbol{\eta}^{\mathbf{htf}}_{\boldsymbol{h_2}}\\ \boldsymbol{\chi}^{\mathbf{htf}}_{\boldsymbol{h_2}}\\ \vdots\\ \boldsymbol{\eta}^{\mathbf{htf}}_{\boldsymbol{h_m}}\\ \boldsymbol{\chi}^{\mathbf{htf}}_{\boldsymbol{h_m}}\end{bmatrix} = \underbrace{\begin{bmatrix}\boldsymbol{A}^{\mathbf{htf}}_{\mathbf{cos},\boldsymbol{h_1}}\\ -\frac{1}{V_{n,h_1}}\boldsymbol{A}^{\mathbf{htf}}_{\mathbf{sin},\boldsymbol{h_1}}\\ \boldsymbol{A}^{\mathbf{htf}}_{\mathbf{cos},\boldsymbol{h_2}}\\ -\frac{1}{V_{n,h_2}}\boldsymbol{A}^{\mathbf{htf}}_{\mathbf{sin},\boldsymbol{h_2}}\\ \vdots\\ \boldsymbol{A}^{\mathbf{htf}}_{\mathbf{cos},\boldsymbol{h_m}}\\ -\frac{1}{V_{n,h_m}}\boldsymbol{A}^{\mathbf{htf}}_{\mathbf{sin},\boldsymbol{h_m}}\end{bmatrix}}_{\boldsymbol{G}^{\mathbf{htf}}_{\boldsymbol{b}}} \begin{bmatrix}\boldsymbol{I} & \boldsymbol{I} & \cdots & \boldsymbol{I}\end{bmatrix} \begin{bmatrix}\boldsymbol{\psi}^{\mathbf{htf}}_{\boldsymbol{h_1}}\\ \boldsymbol{\psi}^{\mathbf{htf}}_{\boldsymbol{h_2}}\\ \vdots\\ \boldsymbol{\psi}^{\mathbf{htf}}_{\boldsymbol{h_m}}\end{bmatrix} \tag{34}$$

$$\begin{bmatrix}\boldsymbol{\Delta}\hat{\boldsymbol{V}}^{\mathbf{htf}}_{\boldsymbol{h_1}}\\ \boldsymbol{\Delta}\hat{\boldsymbol{\theta}}^{\mathbf{htf}}_{\boldsymbol{h_1}}\\ \boldsymbol{\Delta}\hat{\boldsymbol{V}}^{\mathbf{htf}}_{\boldsymbol{h_2}}\\ \boldsymbol{\Delta}\hat{\boldsymbol{\theta}}^{\mathbf{htf}}_{\boldsymbol{h_2}}\\ \vdots\\ \boldsymbol{\Delta}\hat{\boldsymbol{V}}^{\mathbf{htf}}_{\boldsymbol{h_m}}\\ \boldsymbol{\Delta}\hat{\boldsymbol{\theta}}^{\mathbf{htf}}_{\boldsymbol{h_m}}\end{bmatrix} = \underbrace{\begin{bmatrix}k_1h_1\omega_n\boldsymbol{G}^{\mathbf{htf}}_{\mathbf{int}} & \boldsymbol{0} & \boldsymbol{0} & \boldsymbol{0} & \cdots & \boldsymbol{0} & \boldsymbol{0}\\ \boldsymbol{0} & k_1h_1\omega_n\boldsymbol{G}^{\mathbf{htf}}_{\mathbf{int}} + h_1\lambda(\boldsymbol{G}^{\mathbf{htf}}_{\mathbf{int}})^2 & \boldsymbol{0} & \boldsymbol{0} & \cdots & \boldsymbol{0} & \boldsymbol{0}\\ \boldsymbol{0} & \boldsymbol{0} & k_2h_2\omega_n\boldsymbol{G}^{\mathbf{htf}}_{\mathbf{int}} & \boldsymbol{0} & \cdots & \boldsymbol{0} & \boldsymbol{0}\\ \boldsymbol{0} & h_2\lambda(\boldsymbol{G}^{\mathbf{htf}}_{\mathbf{int}})^2 & \boldsymbol{0} & k_2h_2\omega_n\boldsymbol{G}^{\mathbf{htf}}_{\mathbf{int}} & \cdots & \boldsymbol{0} & \boldsymbol{0}\\ \vdots & \vdots & \vdots & \vdots & \ddots & \vdots & \vdots\\ \boldsymbol{0} & \boldsymbol{0} & \boldsymbol{0} & \boldsymbol{0} & \cdots & k_mh_m\omega_n\boldsymbol{G}^{\mathbf{htf}}_{\mathbf{int}} & \boldsymbol{0}\\ \boldsymbol{0} & h_m\lambda(\boldsymbol{G}^{\mathbf{htf}}_{\mathbf{int}})^2 & \boldsymbol{0} & \boldsymbol{0} & \cdots & \boldsymbol{0} & k_mh_m\omega_n\boldsymbol{G}^{\mathbf{htf}}_{\mathbf{int}}\end{bmatrix}}_{\boldsymbol{G}^{\mathbf{htf}}_{\boldsymbol{a}}} \begin{bmatrix}\boldsymbol{\eta}^{\mathbf{htf}}_{\boldsymbol{h_1}}\\ \boldsymbol{\chi}^{\mathbf{htf}}_{\boldsymbol{h_1}}\\ \boldsymbol{\eta}^{\mathbf{htf}}_{\boldsymbol{h_2}}\\ \boldsymbol{\chi}^{\mathbf{htf}}_{\boldsymbol{h_2}}\\ \vdots\\ \boldsymbol{\eta}^{\mathbf{htf}}_{\boldsymbol{h_m}}\\ \boldsymbol{\chi}^{\mathbf{htf}}_{\boldsymbol{h_m}}\end{bmatrix} \tag{35}$$

TABLE II
SOME CASE STUDIES FOR THE STABILITY ASSESSMENT OF THE MSOGI-FLL

Case Studies	SOGI-FLL/DSOGI-FLL/MSOGI-FLL				Single-phase input signal		
	Number of SOGIs	Concerned harmonics	SOGI gains	FLL gain	Nominal frequency	Nominal amplitudes	Nominal phase angles
Case 1	$m=1$	$h_1=1$	$k_1=k/h_1=\sqrt{2}$	$\lambda=49348$ rad/s^2	$\omega_n=2\pi 50$ rad/s	$V_{n,h_1}=1$ p.u.	$\theta_{n,h_1}=h_1\omega_n t+0$
Case 2	$m=2$	$h_1=1$ $h_2=3$	$k_1=k/h_1=\sqrt{2}$ $k_2=k/h_2=\sqrt{2}/3$	$\lambda=49348$ rad/s^2	$\omega_n=2\pi 50$ rad/s	$V_{n,h_1}=1$ p.u. $V_{n,h_2}=0.2$ p.u.	$\theta_{n,h_1}=h_1\omega_n t+0$ $\theta_{n,h_2}=h_2\omega_n t+\pi/3$
Case 3	$m=3$	$h_1=1$ $h_2=3$ $h_3=5$	$k_1=k/h_1=\sqrt{2}$ $k_2=k/h_2=\sqrt{2}/3$ $k_2=k/h_3=\sqrt{2}/5$	$\lambda=49348$ rad/s^2	$\omega_n=2\pi 50$ rad/s	$V_{n,h_1}=1$ p.u. $V_{n,h_2}=0.2$ p.u. $V_{n,h_3}=0.1$ p.u.	$\theta_{n,h_1}=h_1\omega_n t+0$ $\theta_{n,h_2}=h_2\omega_n t+\pi/3$ $\theta_{n,h_3}=h_3\omega_n t+\pi/6$
Case 4	$m=2$	$h_1=1$ $h_2=5$	$k_1=k/h_1=\sqrt{2}$ $k_2=k/h_2=\sqrt{2}/5$	$\lambda=49348$ rad/s^2	$\omega_n=2\pi 50$ rad/s	$V_{n,h_1}=1$ p.u. $V_{n,h_2}=0.2$ p.u.	$\theta_{n,h_1}=h_1\omega_n t+0$ $\theta_{n,h_2}=h_2\omega_n t+\pi/3$

TABLE III
SUMMARY OF PMS AND GMS OF THE CASE STUDIES

	Phase Margin (PM)	Gain Margin (GM)
Case 1	$\mathrm{PM}_1=63.6^\circ$ $\mathrm{PM}_2=80.8^\circ$	$\mathrm{GM}_1=11.9\,\mathrm{dB}$ $\mathrm{GM}_2=\inf$
Case 2	$\mathrm{PM}_1=52.6^\circ$ $\mathrm{PM}_2=84.8^\circ$ $\mathrm{PM}_3=87^\circ$ $\mathrm{PM}_4=89.1^\circ$	$\mathrm{GM}_1=10.2\,\mathrm{dB}$ $\mathrm{GM}_2=22.3\,\mathrm{dB}$ $\mathrm{GM}_4=22.3\,\mathrm{dB}$ $\mathrm{GM}_4=\inf$
Case 3	$\mathrm{PM}_1=50.2^\circ$ $\mathrm{PM}_2=86.3^\circ$ $\mathrm{PM}_3=86.7^\circ$ $\mathrm{PM}_4=88.9^\circ$ $\mathrm{PM}_5=89.3^\circ$ $\mathrm{PM}_6=89.6^\circ$	$\mathrm{GM}_1=9.4\,\mathrm{dB}$ $\mathrm{GM}_2=21.6\,\mathrm{dB}$ $\mathrm{GM}_3=21.6\,\mathrm{dB}$ $\mathrm{GM}_4=36.6\,\mathrm{dB}$ $\mathrm{GM}_5=36.6\,\mathrm{dB}$ $\mathrm{GM}_6=\inf$
Case 4	$\mathrm{PM}_1=62.5^\circ$ $\mathrm{PM}_2=77.5^\circ$ $\mathrm{PM}_3=89.3^\circ$ $\mathrm{PM}_4=89.6^\circ$	$\mathrm{GM}_1=11.8\,\mathrm{dB}$ $\mathrm{GM}_2=32.4\,\mathrm{dB}$ $\mathrm{GM}_3=32.4\,\mathrm{dB}$ $\mathrm{GM}_4=\inf$

reduction becomes more noticeable if a higher number of parallel SOGIs in the MSOGI-FLL structure is considered.

The study in Case 2 demonstrated that adding a SOGI centered at a harmonic frequency in parallel with the SOGI centered at the fundamental frequency has a negative effect on the stability margin. A natural question that arises here is if the center frequency of the parallel SOGI has any effect on the stability margin. To investigate this issue, a different DSOGI-FLL than that in Case 2 is considered (see Case 4 in Table II). Note that the DSOGI-FLL in Case 4 includes two parallel SOGIs centered at the fundamental and fifth-order harmonic frequencies. The open-loop eigenloci of this DSOGI-FLL can be observed in Fig. 6(d). It is observed that it has more descent stability margins compared to the DSOGI-FLL in Case 2 (see Table III). This observation means that the center frequency of the parallel SOGI may have a noticeable effect on stability properties. It also demonstrates that a parallel SOGI centered at lower-orders harmonics has a more negative stability effect than that centered at higher order harmonics.

C. Stability Region in Parameter Space

To further support conclusions made in the previous section, stability regions of the case studies summarized in Table II are obtained and compared. Note that an MSOGI-FLL with m parallel SOGIs has $m+1$ degrees of freedom, i.e., $k_1, k_2, \ldots, k_m$, and λ. Therefore, obtaining the stability region of an MSOGI-FLL in the general case can be complicated. However, as the LTP model in Fig. 3(a) shows, an optimum relationship between the control gains of the parallel SOGIs can be obtained by considering $h_1k_1=h_2k_2=\cdots=h_mk_m=k$. In this way, different estimation loops of the MSOGI configuration will have similar dynamics. This consideration, which was already assumed in Sections II-E and III-B for the model verification and assessing factors affecting the stability margins of the MSOGI-FLL, has been originally suggested in [10]. Based on this selection and also defining the FLL gain λ as $\lambda=k\omega_n\Gamma$, where Γ is a positive factor, one can determine the stability region of an MSOGI-FLL (with an arbitrary number of parallel SOGIs) in the (Γ, k) space using the generalized Nyquist stability criterion [20].

Fig. 7 shows the stability region of the SOGI-FLL, the DSOGI-FLL, and MSOGI-FLL, which are corresponding to Case 1, 2, and 3 in Table II. Note that the largest and smallest stability regions belong to the SOGI-FLL and MSOGI-FLL, respectively, and the stability region of the DSOGI-FLL is somewhere between these two. These observations are completely consistent with the conclusions made in Section III-B. Note also that, in all cases, increasing the value of Γ limits the maximum value of k that ensures stability from the small-signal point of view.

In this stage, it can be interesting to see if changing the working points affects the stability properties of a DSOGI/MSOGI-based system. For the sake of simplicity and brevity, a DSOGI-FLL (see Case 2 in Table II) is considered, and the effect of changing V_{n,h_2} on its stability region is investigated. Fig. 8 shows the obtained results. Note that the area below each curve is the DSOGI-FLL's stability region for its corresponding V_{n,h_2}. It can be observed that the stability region of the DSOGI-FLL becomes smaller by increasing the value of V_{n,h_2}.

IV. CLOSE VARIANTS OF THE MSOGI-BASED SYNCHRONIZATION/SIGNAL PROCESSING SYSTEMS

A. Multiple Inverse Park Transform-Based PLL

1) Description: Using a parallel configuration of SRF low-pass filters (LPFs) rotating at the targeted harmonic frequencies is an alternative to the MSOGI configuration [see Fig. 1(a)] for the synchronization and signal processing purposes in single-phase applications [24]–[26]. This configuration, which is briefly referred to as the multiple inverse park transform (MIPT) structure, can be observed in Fig. 9(a). Note that the

β-axis output of each frame (filter module) is fed back and used as its β-axis input. This action is required for generating an orthogonal signal for transferring information to the *dq* frame. Note also that the α-axis input of each frame is generated by subtracting the α-axis outputs of other frames from the single-phase input signal $v(t)$.

The MIPT structure requires an estimation of the phase angle of the fundamental component, i.e., $\bar{\theta}_{h_1}$, for the Park and inverse Park transformations. Such estimation is most often provided by a basic PLL, as shown in Fig. 9(b) or (c). Note that the only difference between these PLLs is their input signals, which are v_{dq} and $\bar{v}_{dq}$ in Fig. 9(b) and (c), respectively.

2) LTP Modeling: According to Fig. 9(a), the output amplitude and phase angle of the *dq* frame rotating at the fundamental angular speed are

$$\hat{V}_{h_1} = \sqrt{\hat{v}^2_{\alpha,h_1} + \hat{v}^2_{\beta,h_1}} \tag{37}$$

$$\hat{\theta}_{h_1} = \tan^{-1}(\hat{v}_{\beta,h_1}/\hat{v}_{\alpha,h_1}) \tag{38}$$

where

$$\begin{bmatrix}\hat{v}_{\alpha,h_1}\\ \hat{v}_{\beta,h_1}\end{bmatrix} = \begin{bmatrix}\cos(h_1\bar{\theta}_{h_1}) & -\sin(h_1\bar{\theta}_{h_1})\\ \sin(h_1\bar{\theta}_{h_1}) & \cos(h_1\bar{\theta}_{h_1})\end{bmatrix}\begin{bmatrix}\bar{v}_d\\ \bar{v}_q\end{bmatrix}. \tag{39}$$

Differentiating (37) and (38) with respect to time gives

$$\dot{\hat{V}}_{h_1} = \frac{\hat{v}_{\alpha,h_1}\dot{\hat{v}}_{\alpha,h_1} + \hat{v}_{\beta,h_1}\dot{\hat{v}}_{\beta,h_1}}{\hat{V}_{h_1}} \tag{40}$$

$$\dot{\hat{\theta}}_{h_1} = \frac{\dot{\hat{v}}_{\beta,h_1}\hat{v}_{\alpha,h_1} - \dot{\hat{v}}_{\alpha,h_1}\hat{v}_{\beta,h_1}}{\hat{V}^2_{h_1}} \tag{41}$$

where according to (39) and Fig. 9

$$\begin{aligned}\begin{bmatrix}\dot{\hat{v}}_{\alpha,h_1}\\ \dot{\hat{v}}_{\beta,h_1}\end{bmatrix} =& -h_1\hat{\omega}\begin{bmatrix}\sin(h_1\bar{\theta}_{h_1}) & \cos(h_1\bar{\theta}_{h_1})\\ -\cos(h_1\bar{\theta}_{h_1}) & \sin(h_1\bar{\theta}_{h_1})\end{bmatrix}\begin{bmatrix}\bar{v}_d\\ \bar{v}_q\end{bmatrix}\\ &+\begin{bmatrix}\cos(h_1\bar{\theta}_{h_1}) & -\sin(h_1\bar{\theta}_{h_1})\\ \sin(h_1\bar{\theta}_{h_1}) & \cos(h_1\bar{\theta}_{h_1})\end{bmatrix}\begin{bmatrix}\dot{\bar{v}}_d\\ \dot{\bar{v}}_q\end{bmatrix}\end{aligned} \tag{42}$$

$$\begin{bmatrix}\dot{\bar{v}}_d\\ \dot{\bar{v}}_q\end{bmatrix} = \omega_p\begin{bmatrix}v_d - \bar{v}_d\\ v_q - \bar{v}_q\end{bmatrix} \tag{43}$$

$$\begin{bmatrix}v_d\\ v_q\end{bmatrix} = \begin{bmatrix}\cos(h_1\bar{\theta}_{h_1}) & \sin(h_1\bar{\theta}_{h_1})\\ -\sin(h_1\bar{\theta}_{h_1}) & \cos(h_1\bar{\theta}_{h_1})\end{bmatrix}\begin{bmatrix}e + \hat{v}_{\alpha,h_1}\\ \hat{v}_{\beta,h_1}\end{bmatrix}. \tag{44}$$

Using (39), (43), and (44), we can rewrite (42) as

$$\begin{bmatrix}\dot{\hat{v}}_{\alpha,h_1}\\ \dot{\hat{v}}_{\beta,h_1}\end{bmatrix} = \omega_p\begin{bmatrix}e\\ 0\end{bmatrix} + h_1\hat{\omega}\begin{bmatrix}0 & -1\\ 1 & 0\end{bmatrix}\begin{bmatrix}\hat{v}_{\alpha,h_1}\\ \hat{v}_{\beta,h_1}\end{bmatrix}. \tag{45}$$

Note that $e = v - \sum_{i=1}^{m}\hat{v}_{\alpha,h_i}$.

Substituting (45) into (40) and (41) gives

$$\dot{\hat{V}}_{h_1} = \omega_p\frac{\hat{v}_{\alpha,h_1}}{\hat{V}_{h_1}}\left(v - \sum_{i=1}^{m}\hat{v}_{\alpha,h_i}\right) \tag{46}$$

$$\dot{\hat{\theta}}_{h_1} = h_1\hat{\omega} - \omega_p\frac{\hat{v}_{\beta,h_1}}{\hat{V}^2_{h_1}}\underbrace{\left(v - \sum_{i=1}^{m}\hat{v}_{\alpha,h_i}\right)}_{e(t)}. \tag{47}$$

Equations (46) and (47) are the same as (11) and (12), respectively, if $k_1h_1\hat{\omega} = \omega_p$ is considered. Therefore, their linearized versions will also be the same as (15) and (16) if $k_1h_1\omega_n = \omega_p$ is considered [see (48) and (49)]

$$\Delta\dot{\hat{V}}_{h_1} \approx \omega_p\cos(\theta_{n,h_1})\sum_{i=1}^{m}\psi_{h_i} \tag{48}$$

$$\Delta\dot{\hat{\theta}}_{h_1} \approx h_1\Delta\hat{\omega} - \omega_p\frac{\sin(\theta_{n,h_1})}{V_{n,h_1}}\sum_{i=1}^{m}\psi_{h_i}. \tag{49}$$

In a similar manner, the outputs of the *dq* frame rotating at $h_m\bar{\theta}_1$, i.e., $\hat{V}_{h_m}$ and $\hat{\theta}_{h_m}$, can be linearized as

$$\Delta\dot{\hat{V}}_{h_m} \approx \omega_p\cos(\theta_{n,h_m})\sum_{i=1}^{m}\psi_{h_i} \tag{50}$$

$$\Delta\dot{\hat{\theta}}_{h_m} \approx h_m\Delta\hat{\omega} - \omega_p\frac{\sin(\theta_{n,h_m})}{V_{n,h_m}}\sum_{i=1}^{m}\psi_{h_i}. \tag{51}$$

Based on (48)–(51), the LTP model of the MIPT structure can be obtained as shown in Fig. 10. The remaining part is obtaining the linear model of the basic PLLs in Fig. 9, which needs to be linked with that of the MIPT structure.

According to Fig. 9(a), $\bar{v}_d(s) = \frac{\omega_p}{s+\omega_p}v_d(s)$ and $\bar{v}_q(s) = \frac{\omega_p}{s+\omega_p}v_q(s)$. Therefore, we have $v_d(s) = \frac{s+\omega_p}{\omega_p}\bar{v}_d(s)$ and $v_q(s) = \frac{s+\omega_p}{\omega_p}\bar{v}_q(s)$. Considering these, the basic PLL in Fig. 9(b) can be represented as shown in Fig. 11. This PLL has a similar structure to that in Fig. 1(c), which its linearization was presented before in Section II-D. Following a similar procedure, one can linearize this PLL as shown in Fig. 10. Note that the block with the transfer function $\frac{s+\omega_p}{\omega_p}$ in Fig. 10 should be removed if the basic PLL in Fig. 9(c) instead of that in Fig. 9(b) is used. In this case, the MIPT-PLL becomes approximate equivalent to the MSOGI-PLL. To confirm this fact, an experimental comparison between the MSOGI-PLL [see Fig. 1(a) and (c)] and MIPT-PLL [see Fig. 9(a) and (c)] is carried out. This comparison is carried out using a dSPACE 1006 platform and a Chroma grid simulator. Three SOGIs/filter modules centered/rotating at the fundamental, third, and fifth-harmonic frequency are considered in the MSOGI-PLL/MIPT-PLL. The selected control parameters for the MIPT-PLL are $k_p = 130$, $k_i = 7014$, and $\omega_p = 2\omega_n = 628$ rad/s. Obtaining these parameters is based on the symmetrical optimum method [27]. The MSOGI-PLL is also designed to have the same PI control gains as those of the MIPT-PLL, and its SOGI gains are $k_1h_1 = k_2h_2 = k_3h_3 = \omega_p/\omega_n = 2$.

The experimental results are shown in Fig. 12. It is observed that the MIPT-PLL and MSOGI-PLL have very close outputs. These results support the above theoretical predictions.

3) Model Verification: This section aims to evaluate the accuracy of the obtained LTP model for the MIPT-PLL. To this end, a similar procedure as that shown in Fig. 4 is followed. The control parameters of the MIPT-PLL can be observed in Table IV. The nominal values of different components of the single-phase input signal are considered to be the same as those listed in Table I. To save space, only the results of Test 2, which is already defined in Section II-E, are presented. As it can be

TABLE IV
SELECTED CONTROL PARAMETERS FOR THE MODEL VERIFICATION OF THE MIPT-PLL

Number of *dq* frames	Concerned harmonics	LPFs cutoff frequency	PI control gains
$m = 3$	$h_1 = 1, h_2 = 3, h_3 = 5$	$\omega_p = \sqrt{2}\omega_n = 444.3$ rad/s	$k_p = 177$ and $k_i = 15791$

observed in Fig. 13, the MIPT-PLL and its LTP model have very close results. This observation confirms the high accuracy of the LTP model.

In a similar manner as that presented for the case of the MSOGI-FLL in Section III, the open-loop HTF of the MIPT-PLL can be obtained and its stability can be investigated. This investigation is not presented here to save space.

B. Multiple EPLL (MEPLL) System

1) Description: An MEPLL system, as shown in Fig. 14, is the parallel connection of m units [16]. The first unit is the open-loop part of the well-known enhanced PLL (EPLL). Note that the EPLL, which its governing differential equations can be obtained using the gradient descent method [16], is a versatile signal processing tool in different applications [28]–[32]. The units 2 to m are similar to the unit 1. The only difference is that they do not extract the angular frequency of their corresponding frequency components. Instead, they receive an estimation of the fundamental angular frequency from the unit 1 for adapting center frequencies of their voltage-controlled oscillators.[3] The MEPLL is able to decompose a single-phase input signal to its constituent components and estimate their angular frequency, phase angle, and amplitude.

2) LTP Modeling: Using the first unit of the MEPLL system in Fig. 14, we have

$$\dot{\hat{V}}_{h_1} = \mu_1 \cos(\hat{\theta}_{h_1}) \overbrace{\left(v - \sum_{i=1}^{m} \hat{v}_{\alpha,h_i}\right)}^{e} \tag{52}$$

$$\dot{\hat{\theta}}_{h_1} = h_1\hat{\omega} - \frac{\mu_1}{\hat{V}_{h_1}} \sin(\hat{\theta}_{h_1}) \left(v - \sum_{i=1}^{m} \hat{v}_{\alpha,h_i}\right) \tag{53}$$

$$\Delta\dot{\hat{\omega}} = -\frac{\gamma}{\hat{V}_{h_1}} \sin(\hat{\theta}_{h_1}) \left(v - \sum_{i=1}^{m} \hat{v}_{\alpha,h_i}\right). \tag{54}$$

If we compare the above equations with (11), (12), and (19), it is immediate to conclude that they are the same equations if $\lambda = \gamma$ and $k_1 h_1 \hat{\omega} = \mu_1$ are considered.[4] It implies that the EPLL and SOGI-FLL and, therefore, their extended versions (the MSOGI-FLL and MEPLL system) are approximate equivalent and have the same LTP model. The experimental results in Fig. 15 confirm this fact. The only point is that the gain $k_i h_i \omega_n$ $(i = 1, 2, \ldots, m)$ and λ in the LTP model of the MSOGI-FLL need to be replaced by μ_i and γ, respectively. Having the same LTP model means that the MEPLL system has the same open-loop HTF as that obtained for the MSOGI-FLL [see (36)]. It also means that the MEPLL system has the same small-signal stability properties as those of the MSOGI-FLL.

[3]If it is required (for instance, when the estimation of interharmonics is intended), they can estimate the frequency of their corresponding frequency components in a similar manner as the unit 1.

[4]The second condition, i.e., $k_1 h_1 \hat{\omega} = \mu_1$, may not be fully satisfied as $\hat{\omega}$ is a time-varying signal and μ_1 is a constant. However, in power applications, which is the main focus of this work, the input signal frequency, and, therefore, its estimation have a limited range of variation in practice. It implies that the abovementioned condition will be to a good extend satisfied.

V. CONCLUSION

The LTP modeling and stability assessment of the single-phase MSOGI-based synchronization/signal decomposition systems and their close variants were the objective of this article. First, the LTP modeling of the MSOGI-FLL/PLL was conducted, and the accuracy of the obtained LTP model was verified numerically. Focusing on the MSOGI-FLL, it was then shown how the open-loop HTF can be obtained using the LTP model. The stability assessment of the MSOGI-FLL was then conducted using its open-loop HTF. It was demonstrated that increasing the number of parallel SOGIs adversely affects the stability margins and stability region of the MSOGI-FLL. It was also shown that the center frequency of parallel SOGIs has a noticeable stability effect; it was observed that a parallel SOGI centered at lower orders harmonics has a more negative stability effect than that centered at higher order harmonics. It was also found that the working points of frequency components of the single-phase input signal may affect the stability properties of the MSOGI-FLL. The study was then focused on some alternative structures, i.e., the MEPLL system and MIPT-PLL. The MEPLL system was found to be an approximate equivalent of the MSOGI-FLL. Therefore, they have the same LTP model and the same small-signal stability properties. The MIPT structure was also found to be approximate equivalent of the MSOGI structure. Therefore, the MIPT-PLL (depending on its PLL) may be an approximate equivalent of the MSOGI-PLL.

APPENDIX

A. Linearization of $e(t) = \sum_{i=1}^{m} [V_{h_i} \cos(\theta_{h_i}) - \hat{V}_{h_i} \cos(\hat{\theta}_{h_i})]$

Considering the definitions made in (6), the term $e(t)$ can be rewritten as

$$e(t) = \sum_{i=1}^{m} [(V_{n,h_i} + \Delta V_{h_i}) \cos(\theta_{n,h_i} + \Delta\theta_{h_i}) - (V_{n,h_i} + \Delta\hat{V}_{h_i}) \cos(\theta_{n,h_i} + \Delta\hat{\theta}_{h_i})]. \tag{55}$$

Using trigonometric identities, (55) can be approximated by (56) at the top of the next page.

REFERENCES

[1] J. Schiffer, C. A. Hans, T. Kral, R. Ortega, and J. Raisch, "Modeling, analysis, and experimental validation of clock drift effects in low-inertia power systems," *IEEE Trans. Ind. Electron.*, vol. 64, no. 7, pp. 5942–5951, Jul. 2017.

$$e(t) = \sum_{i=1}^{m} \Bigg[\cos(\theta_{n,h_i}) \overbrace{\Big\{ (V_{n,h_i}+\Delta V_{h_i})\cos(\Delta\theta_{h_i}) - (V_{n,h_i}+\Delta\hat{V}_{h_i})\cos(\Delta\hat{\theta}_{h_i}) \Big\}}^{\approx \Delta V_{h_i} - \Delta\hat{V}_{h_i}}$$

$$- \sin(\theta_{n,h_i}) \underbrace{\Big\{ (V_{n,h_i}+\Delta V_{h_i})\sin(\Delta\theta_{h_i}) - (V_{n,h_i}+\Delta\hat{V}_{h_i})\sin(\Delta\hat{\theta}_{h_i}) \Big\}}_{\approx V_{n,h_i}(\Delta\theta_{h_i} - \Delta\hat{\theta}_{h_i})} \Bigg]$$

$$\approx \sum_{i=1}^{m} \underbrace{\Big[(\Delta V_{h_i} - \Delta\hat{V}_{h_i})\cos(\theta_{n,h_i}) - V_{n,h_i}(\Delta\theta_{h_i} - \Delta\hat{\theta}_{h_i})\sin(\theta_{n,h_i}) \Big]}_{\psi_{h_i}} = \sum_{i=1}^{m} \psi_{h_i}. \tag{56}$$

[2] C. M. Hackl and M. Landerer, "Modified second-order generalized integrators with modified frequency locked loop for fast harmonics estimation of distorted single-phase signals," *IEEE Trans. Power Electron.*, vol. 35, no. 3, pp. 3298–3309, Mar. 2020.

[3] U. Nuss, "Blindleistungskompensation mit selbstgeführten stromrichter und kapazitivem energiespeicher," Ph.D. dissertation, Inst. Elect. Eng. (ETI), Karlsruhe Inst. Technol., Karlsruhe, Germany, 1989.

[4] B. Burger and A. Engler, "Fast signal conditioning in single phase systems," in *Proc. Eur. Conf. Power Electron*., 2001, pp. 1–10.

[5] S. Golestan, J. M. Guerrero, F. Musavi, and J. C. Vasquez, "Single-phase frequency-locked loops: A comprehensive review," *IEEE Trans. Power Electron.*, vol. 34, no. 12, pp. 11791–11812, Dec. 2019.

[6] M. Mojiri and A. R. Bakhshai, "Estimation of n frequencies using adaptive notch filter," *IEEE Trans. Circuits Syst. II, Express Briefs*, vol. 54, no. 4, pp. 338–342, Apr. 2007.

[7] M. Mojiri, M. Karimi-Ghartemani, and A. Bakhshai, "Processing of harmonics and interharmonics using an adaptive notch filter," *IEEE Trans. Power Del.*, vol. 25, no. 2, pp. 534–542, Apr. 2010.

[8] M. Mojiri, M. Karimi-Ghartemani, and A. Bakhshai, "Time-domain signal analysis using adaptive notch filter," *IEEE Trans. Signal Process.*, vol. 55, no. 1, pp. 85–93, Jan. 2007.

[9] D. Yazdani, A. Bakhshai, G. Joos, and M. Mojiri, "A real-time extraction of harmonic and reactive current in a nonlinear load for grid-connected converters," *IEEE Trans. Ind. Electron.*, vol. 56, no. 6, pp. 2185–2189, Jun. 2009.

[10] P. Rodriguez, A. Luna, I. Candela, R. Mujal, R. Teodorescu, and F. Blaabjerg, "Multiresonant frequency-locked loop for grid synchronization of power converters under distorted grid conditions," *IEEE Trans. Ind. Electron.*, vol. 58, no. 1, pp. 127–138, Jan. 2011.

[11] P. A. Regalia, "An improved lattice-based adaptive IIR notch filter," *IEEE Trans. Signal Process.*, vol. 39, no. 9, pp. 2124–2128, Sep. 1991.

[12] M. Bodson and S. C. Douglas, "Adaptive algorithms for the rejection of sinusoidal disturbances with unknown frequency," *Automatica*, vol. 33, no. 12, pp. 2213–2221, 1997.

[13] L. Hsu, R. Ortega, and G. Damm, "A globally convergent frequency estimator," *IEEE Trans. Automat. Control*, vol. 44, no. 4, pp. 698–713, Apr. 1999.

[14] M. Mojiri and A. R. Bakhshai, "An adaptive notch filter for frequency estimation of a periodic signal," *IEEE Trans. Automat. Control*, vol. 49, no. 2, pp. 314–318, Feb. 2004.

[15] J. Matas, H. Martin, J. de la Hoz, A. Abusorrah, Y. A. Al-Turki, and M. Al-Hindawi, "A family of gradient descent grid frequency estimators for the SOGI filter," *IEEE Trans. Power Electron.*, vol. 33, no. 7, pp. 5796–5810, Jul. 2018.

[16] M. Karimi-Ghartemani, *Enhanced Phase-Locked Loop Structures for Power and Energy Applications*. Hoboken, NJ, USA: Wiley, 2014.

[17] M. Ciobotaru, R. Teodorescu, and F. Blaabjerg, "A new single-phase PLL structure based on second order generalized integrator," in *Proc. 37th IEEE Power Electron. Specialists Conf.*, 2006, pp. 1–6.

[18] S. Golestan, J. M. Guerrero, and J. C. Vasquez, "Three-phase PLLs: A review of recent advances," *IEEE Trans. Power Electron.*, vol. 32, no. 3, pp. 1894–1907, Mar. 2017.

[19] S. Golestan, J. M. Guerrero, and J. C. Vasquez, "Modeling and stability assessment of single-phase grid synchronization techniques: Linear time-periodic versus linear time-invariant frameworks," *IEEE Trans. Power Electron.*, vol. 34, no. 1, pp. 20–27, Jan. 2019.

[20] S. Golestan, J. M. Guerrero, J. C. Vasquez, A. M. Abusorrah, and Y. Al-Turki, "Standard SOGI-FLL and its close variants: Precise modeling in LTP framework and determining stability region/robustness metrics," *IEEE Trans. Power Electron.*, vol. 36, no. 1, pp. 409–422, Jan. 2021.

[21] S. Foyen, C. Zhang, O. Fosso, and M. Molinas, "Frequency domain modelling for assessment of Hilbert and SOGI based single-phase synchronisation," in *Proc. 45th Annu. Conf. IEEE Ind. Electron. Soc.*, 2019, pp. 1780–1785.

[22] S. Shah, P. Koralewicz, V. Gevorgian, and L. Parsa, "Small-signal modeling and design of phase-locked loops using harmonic signal-flow graphs," *IEEE Trans. Energy Convers.*, vol. 35, no. 2, pp. 600–610, Jun. 2020.

[23] E. Mollerstedt and B. Bernhardsson, "Out of control because of harmonics—An analysis of the harmonic response of an inverter locomotive," *IEEE Control Syst. Mag.*, vol. 20, no. 4, pp. 70–81, Aug. 2000.

[24] S. Golestan, J. M. Guerrero, and J. C. Vasquez, "Single-phase PLLs: A review of recent advances," *IEEE Trans. Power Electron.*, vol. 32, no. 12, pp. 9013–9030, Dec. 2017.

[25] L. Hadjidemetriou, E. Kyriakides, Y. Yang, and F. Blaabjerg, "A synchronization method for single-phase grid-tied inverters," *IEEE Trans. Power Electron.*, vol. 31, no. 3, pp. 2139–2149, Mar. 2016.

[26] L. Hadjidemetriou, Y. Yang, E. Kyriakides, and F. Blaabjerg, "A synchronization scheme for single-phase grid-tied inverters under harmonic distortion and grid disturbances," *IEEE Trans. Power Electron.*, vol. 32, no. 4, pp. 2784–2793, Apr. 2017.

[27] S. Golestan, M. Monfared, F. D. Freijedo, and J. M. Guerrero, "Dynamics assessment of advanced single-phase PLL structures," *IEEE Trans. Ind. Electron.*, vol. 60, no. 6, pp. 2167–2177, Jun. 2013.

[28] M. Karimi-Ghartemani, B. T. Ooi, and A. Bakhshai, "Application of enhanced phase-locked loop system to the computation of synchrophasors," *IEEE Trans. Power Del.*, vol. 26, no. 1, pp. 22–32, Jan. 2011.

[29] H. Zamani, M. Karimi-Ghartemani, and M. Mojiri, "Analysis of power system oscillations from PMU data using an EPLL-based approach," *IEEE Trans. Instrum. Meas.*, vol. 67, no. 2, pp. 307–316, Feb. 2018.

[30] M. Karimi-Ghartemani, H. Mokhtari, M. R. Iravani, and M. Sedighy, "A signal processing system for extraction of harmonics and reactive current of single-phase systems," *IEEE Trans. Power Del.*, vol. 19, no. 3, pp. 979–986, Jul. 2004.

[31] M. Karimi-Ghartemani and J. A. Walseth, "Using the EPLL algorithm as a preprocessor for fault analysis," in *Proc. IEEE 11th Int. Conf. Inf. Sci., Signal Process. Appl.*, 2012, pp. 1377–1382.

[32] S. Golestan, J. Matas, A. M. Abusorrah, and J. M. Guerrero, "More-stable EPLL," *IEEE Trans. Power Electron.*, vol. 37, no. 1, pp. 1003–1011, Jan. 2022.